The Journal of Chemical Physics

Infrared spectroscopy of an endohedral water in fullerene

Cite as: J. Chem. Phys. **154**, 124311 (2021); https://doi.org/10.1063/5.0047350
Submitted: 12 February 2021 • Accepted: 12 March 2021 • Published Online: 29 March 2021

A. Shugai, U. Nagel, Y. Murata, et al.

The Journal of Chemical Physics ARTICLE scitation.org/journal/jcp

Infrared spectroscopy of an endohedral water in fullerene

Cite as: J. Chem. Phys. 154, 124311 (2021); doi: 10.1063/5.0047350
Submitted: 12 February 2021 • Accepted: 12 March 2021 •
Published Online: 29 March 2021

A. Shugai,[1] U. Nagel,[1] Y. Murata,[2] Yongjun Li,[3,a)] S. Mamone,[4] A. Krachmalnicoff,[4] S. Alom,[4] R. J. Whitby,[4] M. H. Levitt,[4] and T. Rõõm[1,b)]

AFFILIATIONS

[1]National Institute of Chemical Physics and Biophysics, Akadeemia tee 23, 12618 Tallinn, Estonia
[2]Institute for Chemical Research, Kyoto University, Kyoto 611-0011, Japan
[3]Department of Chemistry, Columbia University, New York, New York 10027, USA
[4]School of Chemistry, Southampton University, Southampton SO17 1BJ, United Kingdom

[a)]**Present address:** Merck & Co., 126 E Lincoln Ave., Rahway, New Jersey 07065, USA.
[b)]**Author to whom correspondence should be addressed:** toomas.room@kbfi.ee

ABSTRACT

An infrared absorption spectroscopy study of the endohedral water molecule in a solid mixture of $H_2O@C_{60}$ and C_{60} was carried out at liquid helium temperature. From the evolution of the spectra during the *ortho–para* conversion process, the spectral lines were identified as *para*-H_2O and *ortho*-H_2O transitions. Eight vibrational transitions with rotational side peaks were observed in the mid-infrared: ω_1, ω_2, ω_3, $2\omega_1$, $2\omega_2$, $\omega_1 + \omega_3$, $\omega_2 + \omega_3$, and $2\omega_2 + \omega_3$. The vibrational frequencies ω_2 and $2\omega_2$ are lower by 1.6% and the rest by 2.4%, as compared to those of free H_2O. A model consisting of a rovibrational Hamiltonian with the dipole and quadrupole moments of H_2O interacting with the crystal field was used to fit the infrared absorption spectra. The electric quadrupole interaction with the crystal field lifts the degeneracy of the rotational levels. The finite amplitudes of the pure ν_1 and ν_2 vibrational transitions are consistent with the interaction of the water molecule dipole moment with a lattice-induced electric field. The permanent dipole moment of encapsulated H_2O is found to be 0.50 ± 0.05 D as determined from the far-infrared rotational line intensities. The translational mode of the quantized center-of-mass motion of H_2O in the molecular cage of C_{60} was observed at 110 cm^{-1} (13.6 meV).

I. INTRODUCTION

Endohedral fullerenes consist of atoms or molecules fully encapsulated in closed carbon cages. The remarkable synthetic route known as "molecular surgery" has led to the synthesis of atomic endofullerenes $He@C_{60}$[1] and $Ar@C_{60}$[2] and several molecular endofullerene species, including $H_2@C_{60}$,[3] $H_2O@C_{60}$,[4] $HF@C_{60}$,[5] $CH_4@C_{60}$,[6] and their isotopologs.[7–9] It is well established that these endohedral molecules do not form chemical bonds with the carbon cage and rotate freely.[5,10,11] The rotation is further facilitated by the nearly spherical symmetry of the C_{60} cage. The thermal and chemical stability of $A@C_{60}$ opens up the unique possibility of studying the dynamics and the interactions of a small molecule with carbon nano-surfaces. The trapping potential of dihydrogen H_2 has been described with high accuracy using infrared (IR) spectroscopy,[8–12] inelastic neutron scattering (INS),[13] and theoretical calculations.[14] The non-spherical shape of the small molecule and the quantized translational motion of its center of mass lead to coupled rotational and translational dynamics.[10,15,16]

The water-endofullerene $H_2O@C_{60}$ is of particular interest. The encapsulated water molecule possesses rich spatial quantum dynamics. It is an asymmetric-top rotor, supports three vibrational modes, displays nuclear spin isomerism (*para*-water and *ortho*-water), and has electric dipole and quadrupole moments.

Low-temperature dielectric measurements[17] on solid $H_2O@C_{60}$ show that the electric dipole moment of the encapsulated water is reduced to 0.51 ± 0.05 D from the free water value of 1.85 D. The C_{60} carbon cage responds to the endohedral water molecule with

a counteracting induced dipole, resulting in the lower total dipole moment.[18]

The dynamics of isolated or encapsulated single water molecules have been studied before in other environments, such as noble gas matrices, solid hydrogen, and liquid helium droplets. Although the trapping sites in these matrices have high symmetry and allow water rotation, these systems exist only at low temperature[19,20] or for a very short time.[21,22] Water has also been studied in crystalline environments with nano-size cavities. However, in this case, the interactions with the trapping sites inhibit the free rotation of the water molecules.[23–26]

Several spectroscopic techniques have been used to study $H_2O@C_{60}$, including nuclear magnetic resonance (NMR), INS, and IR spectroscopy[4,11,27–29] and time-domain THz spectroscopy.[30] The low-lying rotational states of the encapsulated molecule are found to be very similar to those of an isolated water molecule, with the notable exception of a 0.6 meV splitting in the $J = 1$ rotational state.[11,31] This indicates that the local environment of the water molecule in $H_2O@C_{60}$ has a lower symmetry than the icosahedral point group of the encapsulating C_{60} cage. The splitting has been attributed to the interaction between the electric quadrupole moment of H_2O and the electric field gradients generated by the electronic charge distribution of neighboring C_{60} molecules.[32,33] The merohedral disorder present in solid C_{60} leads to two C_{60} sites with different quadrupolar interactions. This merohedral disorder also leads to splittings of the IR phonons in solid C_{60}.[34] There is also evidence from dielectric measurements that merohedral disorder leads to electric dipolar activity in solid C_{60}.[35]

Confined molecules exhibit quantization of their translational motion ("particle in a box"), in addition to their quantized rotational and vibrational modes. Quantized translational modes have been observed at 60–70 cm^{-1} for water in noble gas matrices.[19,36] However, comparatively, little is known about the center-of-mass translational mode of $H_2O@C_{60}$. The fundamental frequency of the water translation mode in $H_2O@C_{60}$ has been predicted to occur at ~160 cm^{-1}.[16] This relatively high frequency reflects the rather tight confinement of the water molecule in the C_{60} cage.

The energy level separation between the ground *para* rotational state and the lowest *ortho* rotational state in $H_2O@C_{60}$ has been determined to be 2.6 meV (21 cm^{-1}) by INS.[11] This energy level separation corresponds to a temperature of 28 K. The full thermal equilibration of $H_2O@C_{60}$ at temperatures below 30 K, therefore, requires the conversion of *ortho*-water into *para*-water. This conversion process takes between tens of minutes and several hours below 20 K in $H_2O@C_{60}$.[11,17,30,37] The spin isomer conversion is much faster at ambient temperature, with a time constant of about 30 s reported for $H_2O@C_{60}$ dissolved in toluene.[28]

In this paper, we report on a detailed low-temperature far-IR and mid-IR spectroscopic study of $H_2O@C_{60}$ and C_{60} solid mixtures. The IR technique allows us to measure the frequencies of rotational, vibrational, and translational modes and, from the line intensities, to determine the dipole moment of encapsulated water. In addition, the IR spectra reveal the interaction of endohedral water with the electrostatic fields present in solid C_{60}.

The rest of this paper is organized as follows: Section II discusses the sample preparation, the recording procedures of the IR spectra, and the determination of the IR absorption cross sections for different filling factors, temperatures, and *ortho–para* ratios. The quantum mechanical vibrating rotor model for the encapsulated water molecules is introduced in Sec. III A. We include in this model the interactions of the H_2O electric dipole and quadrupole moments with the electrostatic fields present in solid C_{60}. The theory of the IR line intensities is presented in Sec. III B. Section IV presents the measured IR spectra and the fitting of these data by the quantum mechanical model. The results are discussed in Sec. V, followed by a summary in Sec. VI. Appendixes A–C contain a more detailed theory for the interaction of the water molecules with the electrostatic fields and the infrared radiation and more details on the fitting of the experimental data by the quantum mechanical model.

II. METHODS

A. Sample preparation

$H_2O@C_{60}$ was prepared by a multi-step synthetic route known as "molecular surgery."[4,9] The H_2O-filled (number density $N_\bullet$) and empty (number density $N_\circ$) C_{60} were mixed and co-sublimed to produce small solvent-free crystals with a filling factor $f = N_\bullet/(N_\bullet + N_\circ)$. Five samples with filling factors $f = 0.014$, 0.052, 0.10, 0.18, and 0.80 were studied. The powdered samples were pressed into pellets under vacuum. The diameter of sample pellets was 3 mm, and the thickness d varied from 0.2 mm to 2 mm. The thinner samples were used in the mid-IR because of light scattering in the powder sample. The samples were thicker for lower filling factors and thinner for higher filling factors to avoid the saturation of absorption lines in the far-IR.

B. Measurement techniques

The far-IR measurements were done with a Martin–Puplett type interferometer and ^{3}He cooled bolometer from 5 to 200 cm^{-1}, as described in Ref. 11. The IR measurements between 600 and 12 000 cm^{-1} were performed with an interferometer Vertex 80v (Bruker Optics), as described in Ref. 12.

Two methods were used to record the $H_2O@C_{60}$ absorption spectra.

1. Method 1

The intensity through the sample, I_s, was referenced to the intensity through a 3 mm diameter hole, I_0. The sample was allowed to reach *ortho–para* thermal equilibrium at a temperature of 30 or 45 K, and the temperature was rapidly reduced to 10 or to 5 K. The sample spectrum $I_s(t = 0)$ was recorded immediately after the temperature jump. Since the *ortho–para* conversion process is slow, the *ortho* fraction was assumed to be preserved during the T jump, corresponding to the high temperature *ortho* fraction $n_o \approx 0.74$. The absorption coefficient α was calculated from the ratio $Tr = I_s(t = 0)/I_0$ as $\alpha(t = 0) = -d^{-1} \ln[(1 - R)^{-2}\, Tr]$ where the factor $(1 - R)^2$ with $R = (\eta - 1)^2(\eta + 1)^{-2}$ corrects for the losses of radiation, one reflection from the sample front and one from the back face. The refraction index of solid C_{60} was assumed to be given by $\eta = 2$.[38] To identify *para*-water and *ortho*-water absorption peaks, the difference of two spectra was calculated, $\Delta\alpha = \alpha(t = 0) - \alpha(\Delta t)$, where $\alpha(\Delta t)$ is the absorption spectrum measured after the waiting time Δt. Only the *para*-$H_2O@C_{60}$ and *ortho*-$H_2O@C_{60}$ peaks show up in the differential absorption spectra, with the *para*-$H_2O@C_{60}$ and *ortho*-$H_2O@C_{60}$ peak amplitudes having different signs, *ortho* positive and

para negative. This method was used for the far-IR and the mid-IR part of the spectrum.

2. Method 2

The sample was allowed to reach *ortho–para* thermal equilibrium at a temperature of 30 or 45 K, leading to an *ortho*-rich state, as in the first method. The temperature was rapidly reduced to 10 or to 5 K, and a series of spectra were recorded at intervals of a few minutes starting immediately after the T jump, which continued until the *ortho–para* equilibrium was reached. The differential absorption $\Delta\alpha = -d^{-1}\ln[I_s(0)/I_s]$ was calculated, where $I_s(0)$ is the spectrum recorded immediately after the T jump and I_s is the spectrum recorded when the low temperature equilibrium was reached. The equilibrium *ortho* fraction is ~0.01 at 5 K. Method 2 was used for the far-IR part of the spectrum.

C. Line areas and absorption cross sections

The absorption line area $A_{ji}^{(k)}$ was determined by fitting the measured absorption $\alpha_{ji}^{(k)}(\omega)$ with Gaussian lineshape. $|i\rangle$ and $|j\rangle$ are the initial and final states of the transition, and k denotes *para* (k = p) or *ortho* (k = o) species. From these experimental line areas, $A_{ji}^{(k)}$, a temperature and *para* (*ortho*) fraction independent line area $\overline{A_{ji}^{(k)}}$ was calculated,

$$\overline{A_{ji}^{(k)}}(f) = \frac{A_{ji}^{(k)}(f)}{n_k(p_i^{(k)} - p_j^{(k)})}. \tag{1}$$

The population difference of initial and final states, $p_i^{(k)} - p_f^{(k)}$, is given by the sample temperature T, while the *para* (*ortho*) fraction n_k depends on the history of the sample because of the *ortho–para* conversion process. The normalized absorption line area $\langle A_{ji}^{(k)}\rangle$ was determined from the linear fit of $\overline{A_{ji}^{(k)}}(f)$ for each absorption line,

$$\overline{A_{ji}^{(k)}}(f) = f\langle A_{ji}^{(k)}\rangle. \tag{2}$$

Thus, the normalized absorption line area $\langle A_{ji}^{(k)}\rangle$ is the absorption line area of a sample with a filling factor $f = 1$ and spin isomer fraction $n_k = 1$ where all the population is in the initial state, $p_i^{(k)} = 1$. We used $\langle A_{ji}^{(k)}\rangle$ to calculate a synthetic experimental spectrum for the spectral fit with the quantum mechanical model (Sec. IV B).

Furthermore, to compare the absorption cross sections of $H_2O@C_{60}$ in solid C_{60} and free H_2O, a normalized absorption cross section $\langle\sigma_{ji}^{(k)}\rangle$ was obtained as

$$\langle\sigma_{ji}^{(k)}\rangle = \left(\frac{3\sqrt{\eta}}{\eta^2+2}\right)^2 \frac{\sigma_{ji}^{(k)}}{n_k(p_i^{(k)} - p_j^{(k)})} = \left(\frac{3\sqrt{\eta}}{\eta^2+2}\right)^2 \frac{\langle A_{ji}^{(k)}\rangle}{N_{C_{60}}}, \tag{3}$$

where η is the index of refraction of solid C_{60} and $\sigma_{ji}^{(k)}$ is the absorption cross section of an endohedral water molecule [Eq. (20) in Sec. III B]. This $H_2O@C_{60}$ absorption cross section can be compared to the free water normalized cross section $\langle\sigma_{ji}^{(k)}\rangle = \sigma_{ji}^{(k)} n_k^{-1}(p_i^{(k)} - p_j^{(k)})^{-1}$, where $p_i^{(k)} - p_j^{(k)}$ and $n_k(T)$ are given by the temperature of the water vapor in the experiment reporting $\sigma_{ji}^{(k)}$.

III. THEORY

A. Quantum mechanical model of $H_2O@C_{60}$: Confined vibrating rotor in an electrostatic field

We use the following Hamiltonian to model the endohedral water molecule in solid C_{60}:

$$\mathscr{H} = \mathscr{H}_M + \mathscr{H}_{ES} + \mathscr{H}_T, \tag{4}$$

where $\mathscr{H}_M = \mathscr{H}_v + \mathscr{H}_{rot}$ is the free-molecule rovibrational Hamiltonian and $\mathscr{H}_{ES}$ is the electrostatic interaction of H_2O with the surrounding electric charges. The translational Hamiltonian $\mathscr{H}_T$ consists of water center-of-mass kinetic and potential energies in the molecular cavity of the C_{60} molecule.

We neglect couplings between vibrational modes and between vibrational and rotational modes. In addition, the coupling between the translational motion and rotations is neglected. In $\mathscr{H}_{ES}$, terms describing the coupling of the solid C_{60} crystal field to the electric dipole and quadrupole moments of H_2O are included.

The fitting of IR absorption spectra (Sec. IV B) is done with the Hamiltonian where the translational part is excluded,

$$\mathscr{H} = \mathscr{H}_M + \mathscr{H}_{ES}. \tag{5}$$

We employ three coordinate frames. The space-fixed coordinate frame is denoted A. $M = \{x, y, z\}$ is the molecule-fixed coordinate frame (Fig. 1). The Euler angles $\Omega_{A\to M}$[39,40] transform A to M. The crystal coordinate frame is $C = \{x', y', z'\}$ with the z' axis along the threefold symmetry axis of the S_6 point group, the symmetry group of the C_{60} site in solid C_{60}. The Euler angles $\Omega_{A\to C}$ transform A to C and $\Omega_{C\to M}$ transform C to M. The coordinate systems A and C are used because the radiation interacting with the molecule is defined in the space-fixed coordinate frame A, while the local electrostatic fields are defined by the crystal coordinate frame C, which in a powder sample has a uniform distribution of orientations relative to the space-fixed frame A.

1. Vibrations

H_2O has three normal vibrations: the symmetric stretch of O–H bonds, denoted by the quantum number v_1, the bending motion of the H–O–H bond angle, v_2, and the asymmetric stretch of O–H bonds, v_3,[40] as sketched in Fig. 1(b). The vibrational state is denoted $|\mathbf{v}\rangle$, where the symbol $\mathbf{v}$ denotes the three vibrational quantum numbers, $\mathbf{v} \equiv v_1 v_2 v_3$, each of which takes values $v_i \in \{0, 1, 2, \ldots\}$. The vibrational energy for a harmonic vibrational potential is

$$E_{\mathbf{v}} = \sum_{i=1}^{3} \omega_i\left(v_i + \frac{1}{2}\right),\ v_i = 0, 1,\ 2,\ \ldots, \tag{6}$$

where ω_i is the vibrational frequency of the ith vibration mode, $i \in \{1, 2, 3\}$ and $[\omega_i] = \mathrm{cm}^{-1}$. Throughout this paper, the reported ω_i is the distance between the vibrational energy levels and is assumed to include anharmonic corrections.

2. Rotations

H_2O has the rotational properties of an asymmetric top with principal moments of inertia $I_a < I_b < I_c$.[40] The rotational states are

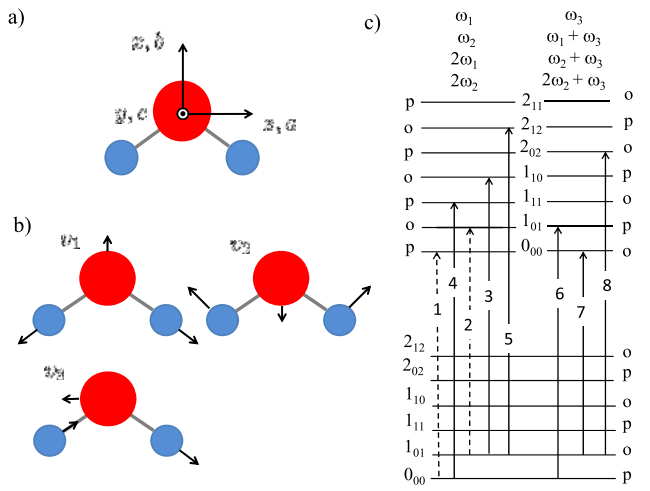

FIG. 1. (a) Molecule-fixed coordinate frame $M = \{x, y, z\}$ and axes of principal moments of inertia, $\{a, b, c\}$. (b) Vibrations: ν_1, symmetric stretch; ν_2, symmetric bend; and ν_3, asymmetric stretch. (c) *para*-water and *ortho*-water rotational energy levels in the ground and excited vibrational states (see Sec. III A 5) and rovibrational IR transitions (arrows) between the levels. The rotational states are labeled by $J_{K_aK_c}$ and p (*para*) and o (*ortho*). The IR transitions are between the *para* states or between the *ortho* states. 1, 3, and 5 are *ortho*-H_2O transitions, and 2 and 4 are *para*-H_2O transitions. Transitions 1 and 2 are forbidden for a free water molecule. The transitions where the one-quantum excitation of the asymmetric stretch vibration ν_3 is involved are numbered 6 (*para*-H_2O), and 7 and 8 (*ortho*-H_2O transitions). The rotational and translational far-IR transitions in the ground vibrational states are shown in the inset of Fig. 2.

indexed by three quantum numbers $J_{K_aK_c}$, where $J = 0, 1, 2, \ldots$, is the rotational angular momentum quantum number. K_a and K_c are the absolute values of the projection of J onto the a and c axes, in the limits of a prolate ($I_a = I_b$) and an oblate ($I_b = I_c$) top, respectively, $K_a, K_c \le J$.[40] Each rotational state $|J_{K_aK_c}, m\rangle$ is $(2J + 1)$-fold degenerate, where $m \in \{-J, -J + 1, \ldots, J\}$ is the projection of $\mathbf{J}$ onto the z' axis of the crystal coordinate frame C.

The energies and the wavefunctions, $|J_{K_aK_c}, m\rangle$, of the free rotor Hamiltonian $\mathscr{H}_{\rm rot}$ depend on the rotational constants of an asymmetric top, $A_{\mathbf{v}} > B_{\mathbf{v}} > C_{\mathbf{v}}$,[40]

$$\mathscr{H}_{\rm rot} = A_{\mathbf{v}}\hat{J}_a^2 + B_{\mathbf{v}}\hat{J}_b^2 + C_{\mathbf{v}}\hat{J}_c^2, \tag{7}$$

where $\hat{J}_i$ are the components of the angular momentum operator $\hat{\mathbf{J}}^2$ along the principal directions a, b, and c. The index $\mathbf{v}$ labels the rotational constants in the vibrational state $|\mathbf{v}\rangle$.

A molecule-fixed coordinate system M (axes x, y, and z, Fig. 1) with its origin at the nuclear center of mass is defined with the following orientations relative to the principal axes of the inertial tensor: $\mathbf{x} \parallel \mathbf{b}$, $\mathbf{y} \parallel \mathbf{c}$, and $\mathbf{z} \parallel \mathbf{a}$, where $\mathbf{y}$ is perpendicular to the H–O–H plane and $\mathbf{x}$ points toward the oxygen atom. The rotational wavefunctions of an asymmetric top in that basis are[39,40]

$$\begin{aligned} |J, k, m, \pm\rangle &= (|J, k, m\rangle \pm |J, -k, m\rangle)/\sqrt{2}, \\ |J, 0, m, \pm\rangle &\equiv |J, 0, m\rangle \text{ if } \quad k = 0, \end{aligned} \tag{8}$$

where k is the projection of $\mathbf{J}$ on the a axis, axis z of M; for $k > 0$, $k \in \{1, 2, \ldots, J\}$ and each state is doubly degenerate. Here, $|J, k, m\rangle$ denotes a normalized rotational function,

$$|J, k, m\rangle = \sqrt{\frac{2J+1}{8\pi^2}}\left[D^J_{mk}(\Omega_{C\to M})\right]^*, \tag{9}$$

where the Euler angles $\Omega_{C\to M}$ transform the crystal-fixed coordinate frame C into the molecule-fixed coordinate frame M and $D^J_{mk}(\Omega)$ is the Wigner rotation matrix element or the Wigner D-function.[39,41]

The correspondence between the asymmetric top wavefunctions $|J, k, m, \pm\rangle$ [Eq. (8)] and the asymmetric top wavefunctions $|J_{K_aK_c}, m\rangle$ is given in Ref. 40. The latter notation of wavefunctions is useful for the symmetry analysis and can be used to relate the wavefunction to *para* and *ortho* states of the water molecule (see Sec. III A 5) and to define the electric dipole transition selection rules [Eqs. (26) and (27)].

3. Electrostatic interactions

We assume two contributions to the electrostatic interaction,

$$\mathscr{H}_{\rm ES} = \mathscr{H}_{\rm Q} + \mathscr{H}_{\rm ed}, \tag{10}$$

denoting the coupling of the quadrupole and dipole moments of H_2O to the corresponding multipole fields created by the surrounding charges.

a. Quadrupolar interaction. It was shown by Felker *et al.*[32] that C_{60} molecules in neighboring lattice sites generate an electric field gradient at the center of a given C_{60} molecule. In $H_2O@C_{60}$, the electric field gradient couples to the electric quadrupole moment of the water molecule, lifting the threefold degeneracy of the $J = 1$ *ortho*-H_2O rotational ground state.[32]

The quadrupolar Hamiltonian may be expanded in rank-2 spherical tensors as follows:[39–42]

$$\mathscr{H}_{\rm Q} = \sum_{m=-2}^{2} (-1)^m V^{(2)}_{-m} Q^C_m, \tag{11}$$

where $\{V^{(2)}_m\}$ are the spherical components of the electric field gradient tensor and $\{Q^C_m\}$ are the quadrupole moments of the water molecule, both expressed in the crystal-fixed coordinate frame C.

The experimental value of the H_2O quadrupole moment in the molecule-fixed coordinate frame M is given by $\{Q_{xx}, Q_{yy}, Q_{zz}\} = \{-0.13, -2.50, 2.63\}$ esu × cm^2.[43] Since $|Q_{xx}| \ll |Q_{yy}|, |Q_{zz}|$, it holds that $Q_{zz} \approx -Q_{yy}$, and we may approximate the water quadrupole moment in spherical coordinates as follows:

$$\begin{aligned} \{Q^M_m\} &= \left\{\frac{1}{2}(Q_{xx} - Q_{yy}), 0, \sqrt{\frac{3}{2}}Q_{zz}, 0, \frac{1}{2}(Q_{xx} - Q_{yy})\right\} \\ &\approx Q_{zz}\left\{\frac{1}{2}, 0, \sqrt{\frac{3}{2}}, 0, \frac{1}{2}\right\}, \quad m = -2, \ldots, +2. \end{aligned} \tag{12}$$

The site symmetry of the C_{60} molecule in solid C_{60} is S_6, with the threefold symmetry axis along the cubic [111] axis, which is chosen here to be the z' axis of the crystal coordinate frame C. The spherical tensor component in frame C is

$$\{V^{(2)C}_m\} = V_{\rm Q}\{0, 0, 1, 0, 0\}, \tag{13}$$

where $m \in \{-2, -1, 0, 1, 2\}$ transforms like the fully symmetric A_g irreducible representation of the point group S_6.[44] After the transformation of the quadrupole moment (12) from the H_2O-fixed molecular frame M to the crystal frame C [see Eq. (A5)], the quadrupolar Hamiltonian (11) is given by

$$\mathscr{H}_{\rm Q} = V_{\rm Q} Q_{zz} \left[\sqrt{\frac{3}{2}} \left[D^2_{00}(\Omega_{C\to M}) \right]^* + \frac{1}{2} \left[D^2_{0,-2}(\Omega_{C\to M}) + D^2_{02}(\Omega_{C\to M}) \right]^* \right]. \quad (14)$$

b. Dipolar interaction. Dielectric measurements of solid C_{60} have provided evidence for the existence of electric dipoles in solid C_{60}.[35] We propose that these electric dipoles are the source of finite electric fields at the C_{60} cage centers.

Consider a crystal electric field $\mathscr{E}$ with spherical coordinates $\{\mathscr{E}, \phi_E, \theta_E\}$ in the crystal-fixed frame C; see Appendix A. For simplicity, we assume a homogeneous crystal field with uniform orientation in the crystal-fixed frame. The interaction of the electric dipole moment with the electric field is given by

$$\begin{aligned} \mathscr{H}_{\rm ed} &= -\sum_{m=-1}^{1} (-1)^m \mathscr{E}^E_{-m} \mu^E_m \\ &= -\sum_{m'=-1}^{1} \mathscr{E} \left[D^1_{0m'}(\Omega_{E\to C}) \right]^* \\ &\quad \times \left[\sum_{m''=-1}^{1} \left[D^1_{m'm''}(\Omega_{C\to M}) \right]^* \mu^M_{m''} \right], \end{aligned} \quad (15)$$

where the dipole moment in the molecule-fixed frame M is given by

$$\{\mu^M_m\} = \frac{\mu_x}{\sqrt{2}} \{-1, 0, 1\}, \quad m \in \{-1, 0, 1\}, \quad (16)$$

where μ_x is the permanent dipole moment of water in the Cartesian coordinates of frame M [Fig. 1(a)]. Since there are no other anisotropies than the axially symmetric electric field gradient tensor, the angle ϕ_E is arbitrary and we choose $\phi_E = 0$.

The Hamiltonian (5) is diagonalized using the basis (8) up to $J \le 4$ for the ground vibrational state $|000\rangle$ and for the three excited vibrational states $|100\rangle$, $|010\rangle$, and $|001\rangle$. The ground state and the three excited vibrational states are assumed to have independent rotational constants $A_{\mathbf{v}}$, $B_{\mathbf{v}}$, and $C_{\mathbf{v}}$, where $\mathbf{v} = 000$, 100, 010, or 001.

After separation of coordinates (see Appendix B 2), the quadrupole and dipole moments in Eqs. (14) and (15) are replaced by their expectation values, $\langle \mathbf{v}|Q^M_0|\mathbf{v}\rangle$, $\langle \mathbf{v}|Q^M_{\pm 2}|\mathbf{v}\rangle$, and $\langle \mathbf{v}|\mu^M_{\pm 1}|\mathbf{v}\rangle$, in the ground and in the three excited vibrational states. We assume for simplicity that the dipole and quadrupole moments of H_2O are independent of the vibrational state $|\mathbf{v}\rangle$.

4. Confined water translations: Spherical oscillator

The translational motion is the center-of-mass motion and is quantized for a confined molecule. The high icosahedral symmetry of the C_{60} cavity is close to spherical symmetry, and therefore, the translational motion of the trapped molecule can be described by the three-dimensional isotropic spherical oscillator model.[45] For simplicity, we write the potential in the harmonic approximation as[42]

$$V(R) = V_2 R^2, \quad (17)$$

where R is the displacement of the H_2O center of mass from the C_{60} cage center. The C_{60} cage is assumed rigid, and its center of mass is fixed.

The frequency of the spherical harmonic oscillator is

$$\omega^0_{\rm t} = \sqrt{2V_2/m}, \quad (18)$$

where m is the mass of a molecule moving in the potential and $[\omega^0_{\rm t}] = \text{rad s}^{-1}$. The energy of the spherical harmonic oscillator is quantized,

$$E_N = \hbar\omega^0_{\rm t} \left(N + \frac{3}{2} \right), \quad (19)$$

where N is the translational quantum number, $N \in \{0, 1, 2, \ldots\}$. The orbital quantum number L takes values $L = N, N-2, \ldots, 1(0)$ for odd (even) N. The energy of the harmonic spherical oscillator does not depend on L, and in the isotropic approximation, there is an additional degeneracy of each E_N level in quantum number M_L, taking $2L + 1$ values, $M_L \in \{-L, -L+1, \ldots, L\}$.

5. Nuclear spin isomers: para-water and ortho-water

The Pauli principle requires that the total quantum state is antisymmetric with respect to exchange of the two protons in water, which as spin-1/2 particles are fermions. This constraint leads to the existence of two nuclear spin isomers, with total nuclear spins $I = 0$ (*para*-H_2O) and $I = 1$ (*ortho*-H_2O), and different sets of rovibrational states. The antisymmetric nature of the quantum state has consequences on the IR spectra: only *para* to *para* and *ortho* to *ortho* transitions are allowed.

The *ortho*-H_2O states have odd values of $K_a + K_c$, while the *para*-H_2O states have even values of $K_a + K_c$ in the ground vibrational state $|000\rangle$; see Fig. 1(c). The allowed rotational transitions are depicted in the inset of Fig. 2(a). The same rule applies to the excited vibrational states $|100\rangle$ and $|010\rangle$ [Fig. 1(c), upper left part]. However, the rules are inverted for the states $|001\rangle$, $|101\rangle$, and $|011\rangle$, which involve one-quantum excitation of the asymmetric stretch mode ν_3. In these cases,[40] *para*-H_2O has odd values of $K_a + K_c$, while *ortho*-H_2O has even values of $K_a + K_c$ [Fig. 1(c), upper right part].

The energy difference between the lowest *para* rotational state $|0_{00}\rangle$ and the lowest *ortho* rotational state $|1_{01}\rangle$ is 2.6 meV (28 K).[11] Above 30 K, the ratio of *ortho* and *para* molecules is $n_o/n_p \approx 3$. Hence, if the sample is cooled rapidly to 4 K, the number of *para* molecules slowly grows in the subsequent time interval, while the number of *ortho* molecules slowly decreases to the thermal equilibrium value $n_o \approx 0$. The full conversion takes several hours.[11,17,30,37]

B. Absorption cross section of $H_2O@C_{60}$

The strengths of the transitions between the rotational states of a polar molecule are determined by the permanent electric dipole moment of the molecule and by the electric field of the infrared radiation, corrected by the polarizability of the medium. In principle, the polarizability χ of the solid depends on the fraction f of C_{60} cages

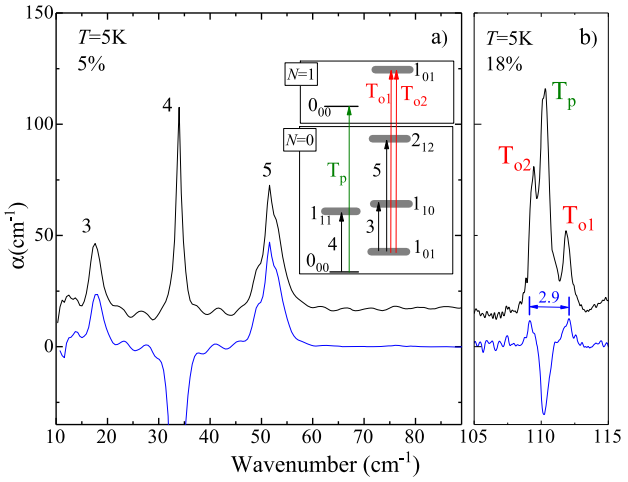

FIG. 2. Far-IR absorption spectra of $H_2O@C_{60}$ at 5 K. (a) Spectrum $\alpha(0)$ was measured after the temperature jump from 30 to 5 K (black), and the difference $\Delta\alpha = \alpha(0) - \alpha(\Delta t)$ was measured Δt = 44 h later (blue). The sample filling factor f = 0.05. Water rotational transitions corresponding to the absorption lines numbered 3 and 5 (*ortho*-water) and 4 (*para*-water) are shown in the inset. (b) Spectrum $\alpha(0)$ was measured after the temperature jump from 30 to 5 K (black), and the difference $\Delta\alpha = \alpha(0) - \alpha(\Delta t)$ was measured Δt = 5 h later (blue). The sample filling factor f = 0.18. The translational transitions $N = 0 \rightarrow N = 1$ for *para* (T_p) and *ortho* (T_{o1}, T_{o2}) $H_2O@C_{60}$ are shown in the inset of panel (a). N is the quantum number of the spherical harmonic oscillator [Eq. (19)].

that contain a water molecule, $\chi(f) = \chi_{C_{60}} + f\chi_{H_2O@C_{60}}$. However, we found that, within the studied range of filling factors, f = 0.1–0.8, the absorption cross section of $H_2O@C_{60}$ was independent of f. Hence, only the polarizability of solid C_{60} is relevant, $\chi \approx \chi_{C_{60}}$, and the problem is similar to the optical absorption of an isolated impurity atom in a crystal.[46]

Following Ref. 46, the electric field in the molecule embedded into the medium with an index of refraction η is $\mathscr{E}_{\text{eff}} = \mathscr{E}(\eta^2 + 2)/3$, where $\mathscr{E}$ is the electric field of radiation in the vacuum. The refractive index of solid C_{60} is $\eta = 2$, [47] and hence, $\mathscr{E}_{\text{eff}} = 2\mathscr{E}$.

In the following discussion, we use the index $k \in \{o, p\}$ to indicate the *ortho* or *para* nuclear spin isomers. The absorption cross section[40] for a given nuclear spin isomer k, including the effective field correction, is given by

$$\sigma_{ji}^{(k)} = N_k^{-1} \int_{\text{Line}} \alpha_{ji}^{(k)}(\omega)\mathrm{d}\omega = \frac{2\pi^2}{h\varepsilon_0 c_0 \eta}\left(\frac{\eta^2+2}{3}\right)^2 \omega_{ji}^{(k)}\left(p_i^{(k)} - p_j^{(k)}\right)S_{ji}^{(k)}, \tag{20}$$

where c_0 is the speed of light in the vacuum and ε_0 is the permittivity of vacuum; SI units are used, and the frequency ω is in number of waves per meter, $[\omega] = \text{m}^{-1}$. The integral in (20) is the area of the absorption line of the transition from the state $|i\rangle$ to $|j\rangle$.

The square of the electric dipole matrix element is given by

$$S_{ji}^{(k)} = \frac{1}{3}\sum_{\sigma=-1}^{1} |\langle j|\mu_\sigma^C|i\rangle|^2, \tag{21}$$

where $|i\rangle$ and $|j\rangle$ are the eigenstates with corresponding energies $E_i^{(k)}$ and $E_j^{(k)}$. The symbol μ_σ^C denotes the dipole moment components of a water molecule in the crystal-fixed frame C. This form of $S_{ji}^{(k)}$ is valid for random orientation of crystals in the powder sample and does not depend on the polarization of light; see Appendix B.

The absorption cross section $\sigma_{ji}^{(k)}$ was evaluated separately for *para*-water and *ortho*-water. The concentration of molecules is $N_k = f N_{C_{60}} n_k$, where n_k is the *ortho* (or *para*) fraction and $n_p + n_o = 1$. The filling factor is denoted by f, and the number density of C_{60} molecules in solid C_{60} is given by $N_{C_{60}} = 1.419 \times 10^{21}\ \text{cm}^{-3}$.[48]

$p_i^{(k)}$ and $p_j^{(k)}$ are the probabilities that the initial and final states are thermally populated,

$$p_n^{(k)} = \left(Z^{(k)}\right)^{-1} \exp\left(-\frac{E_n^{(k)} - E_0^{(k)}}{k_B T}\right), \tag{22}$$

where the statistical sum is

$$Z^{(k)} = \sum_n \exp\left(-\frac{E_n^{(k)} - E_0^{(k)}}{k_B T}\right) \tag{23}$$

and $E_0^{(k)}$ is the ground state energy of *para* (*ortho*) molecules. At the low temperatures considered in this work, only the vibrational ground state is significantly populated. Thus, the significantly thermally populated states are rotational states in the ground vibrational states, which can be written as linear combinations of basis states in Eq. (8). Since we expect that the water molecule is not in a spherically symmetric environment in $H_2O@C_{60}$, the degeneracy in quantum number m is lifted, in general. Therefore, $p_n^{(k)}$ is the thermal population of a non-degenerate rotational state, and the eigenstates $|i\rangle$ and $|j\rangle$ in Eq. (21) include all possible m values for a given J.

When thermal equilibrium is reached between *para*-water and *ortho*-water, the fraction of the nuclear spin isomer k is

$$n_k(T) = \frac{g^{(k)}Z^{(k)}\exp\left(\frac{E_0^{(p)} - E_0^{(k)}}{k_B T}\right)}{g^{(p)}Z^{(p)} + g^{(o)}Z^{(o)}\exp\left(\frac{E_0^{(p)} - E_0^{(o)}}{k_B T}\right)}. \tag{24}$$

For the spin isomer k, the nuclear spin degeneracy $g^{(k)} = 2I + 1$, with $I = 0$ for *para* and $I = 1$ for *ortho*.

The absorption line areas are calculated from Eq. (20), where the matrix elements in Eq. (21) are between the eigenstates $|\Phi_{\text{rot}}^{v}\rangle$ of the Hamiltonian given by Eq. (5). After separation of coordinates (see Appendix B 2), the matrix elements in the crystal-fixed coordinate frame C are

$$\langle j|\mu_\sigma^C|i\rangle = \sum_{\sigma'=-1}^{1} \left\langle \Phi_{\text{rot}}^{v'}\middle| D_{\sigma\sigma'}^{1}(\Omega_{C\to M})^* \middle|\Phi_{\text{rot}}^{000}\right\rangle \langle \mathbf{v}'|\mu_{\sigma'}^M|000\rangle, \tag{25}$$

where the initial state is $|i\rangle = |000\rangle|\Phi_{\text{rot}}^{000}\rangle$ and $|\Phi_{\text{rot}}^{\mathbf{v}}\rangle$ are the linear combinations of states (8). The dipole moments $\langle \mathbf{v}'|\mu_{\sigma'}^M|000\rangle$ are given by Eqs. (B13) and (B14) in Cartesian coordinates.

The following selection rules hold for the electric dipole moment along the z axis (the transition dipole moment of asymmetric stretch ν_3) and along the x axis (the permanent dipole moment and the transition dipole moments of ν_1 and ν_2):[40]

$$\Delta K_a = \text{even}, \quad \Delta K_c = \text{odd} \quad \text{if} \quad \mu_z^M, \tag{26}$$

$$\Delta K_a = \text{odd}, \quad \Delta K_c = \text{odd} \quad \text{if} \quad \mu_x^M, \tag{27}$$

where the convention of molecular axes is as shown in Fig. 1(a) and the definition of dipole moments is given by Eqs. (B13) and (B14). Corresponding transitions are sketched in Figs. 1(c) and 2.

IV. RESULTS AND INTERPRETATION OF SPECTRA

A. Spectra

The water IR absorption lines were identified unambiguously by taking advantage of the slow *ortho–para* conversion at low temperature. After rapid cooling from 30 K to 5 K, the slow *ortho–para* conversion causes the intensity of the *para* lines to slowly increase, while the intensity of the *ortho* lines decreases. The water absorption lines are readily identified and assigned to one of the two spin isomers, by taking the difference between spectra acquired shortly after cooling and spectra acquired after an equilibration time at the lower temperature.

A group of H_2O lines, numbered 3, 4, and 5, is seen below 60 cm^{-1} [Fig. 2(a)]. These far-IR absorption lines have been reported earlier and correspond to the rotational transitions of H_2O in the C_{60} cage.[11] The rotational energy levels involved are shown in the inset of Fig. 2(a). Lines 3 and 5 are *ortho*-water rotational transitions starting from the *ortho*-water ground state $|1_{01}\rangle$. Line 4 is the *para*-water transition from the ground rotational state $|0_{00}\rangle$. No other rotational transitions were observed at 5 K, which is consistent with the selection rules for the electric dipole allowed rotational transitions from states $|0_{00}\rangle$ and $|1_{01}\rangle$.[40]

Further H_2O lines are observed around 110 cm^{-1} [Fig. 2(b)] and in six spectral regions above 600 cm^{-1}, as shown in Figs. 3–6. Below, we address each wavenumber range separately and assign the spectral lines to the transitions shown in the energy schemes of Figs. 1(c) and 2(a). The absorption lines associated with transitions of free water, labeled 1–8, are listed in Table I. Line assignments are supported by the results of spectral fitting using the model of a vibrating rotor in a crystal field.

1. Translational transitions

A group of absorption lines around 110 cm^{-1} is shown in Fig. 2(b). These lines do not correspond to any known water rotational transitions. We assign these peaks to the translational transitions ($N = 0 \rightarrow N = 1$) of *para*-H_2O and *ortho*-H_2O, corresponding to the quantized center-of-mass vibrational motions of the water molecules in the encapsulating C_{60} cages. Here, N denotes the quantum number of a spherical harmonic oscillator.[42]

The assignment of these peaks to water center-of-mass translational oscillations is supported by the presence of lines at 1680 cm^{-1}, visible in the difference spectrum shown in the right-hand side inset of Fig. 3. These lines are 110 cm^{-1} higher than the vibrational transitions 1 and 2 of the ν_2 mode and correspond to the simultaneous excitation of the ν_2 vibration and the translational modes. A similar combination has been observed in $H_2@C_{60}$ where a group of lines between 4240 and 4270 cm^{-1} is the translational sideband to the H_2 stretching vibration.[10]

The translational side peak of the ν_1 vibrational mode is expected at about 3683 cm^{-1}. However, this frequency coincides

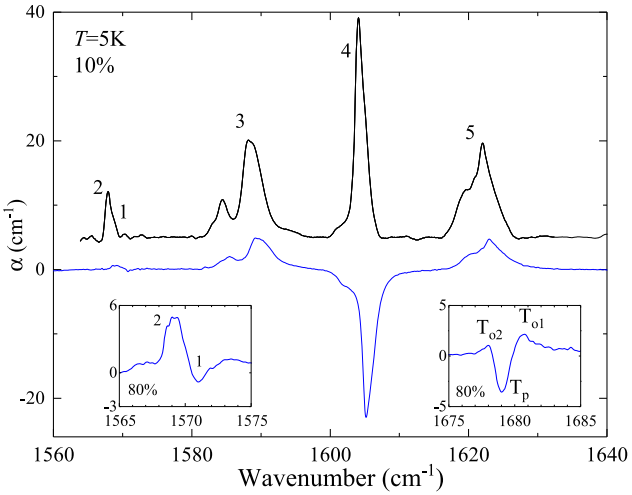

FIG. 3. Absorption spectra of $H_2O@C_{60}$ vibrational, rovibrational, and vibration–translational transitions of the bending vibration ν_2 at 5 K. The spectrum $\alpha(0)$ was measured after the temperature jump from 30 to 5 K (black), and the difference $\Delta\alpha = \alpha(0) - \alpha(\Delta t)$ was measured Δt = 3 h later (blue). The sample filling factor f = 0.1. Lines numbered 1 and 2 are pure vibrational transitions and 3–5 are rovibrational transitions [Fig. 1(c)]. The left inset shows the *para*, line 1, and *ortho*, line 2, components of the pure vibrational transition difference spectrum with time delay 1 h of the f = 0.8 sample. The differential spectrum of ν_2 vibration–translational transitions T_p, T_{o1}, and T_{o2}, at 110 cm^{-1} higher frequency from 1 to 2, is shown in the right inset.

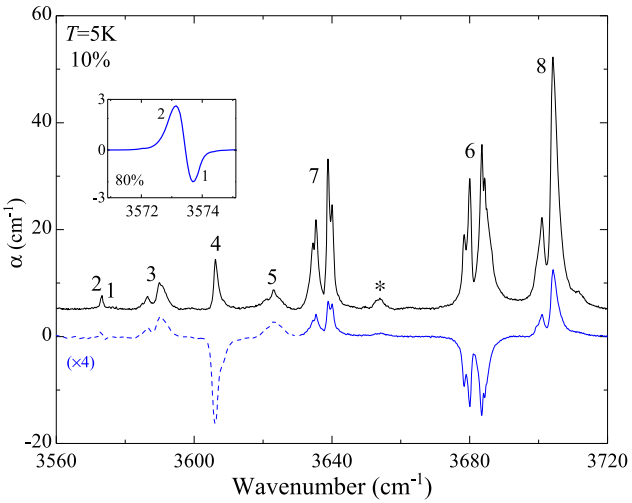

FIG. 4. Absorption spectra of $H_2O@C_{60}$ vibrational, rovibrational, and vibration–translational transitions of symmetric stretching, ν_1, and anti-symmetric stretching, ν_3, vibrations at 5 K. The spectrum $\alpha(0)$ was measured after the temperature jump from 30 to 5 K (black), and the difference $\Delta\alpha = \alpha(0) - \alpha(\Delta t)$ was measured Δt = 3 h later (blue dashed line multiplied by 4 and blue line). The sample filling factor f = 0.1. Lines numbered 1 and 2 are pure vibrational transitions and 3–5 are rovibrational transitions of mode ν_1, and lines 6–8 are rovibrational transitions of ν_3 [Fig. 1(c)]. (∗) marks the ν_3 rovibrational transition at 3654 cm^{-1} from the thermally excited rotational state $|000\rangle|1_{10}\rangle$ to the rovibrational state $|001\rangle|1_{11}\rangle$. The inset shows the *para*, line 1, and *ortho*, line 2, components of the pure vibrational transition of mode ν_1 of the f = 0.8 sample as the difference spectrum with time delay 1 h.

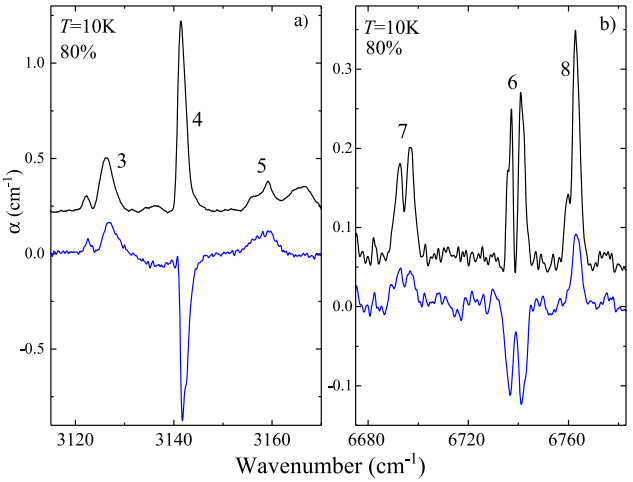

FIG. 5. Absorption spectra of $H_2O@C_{60}$ at 10 K. (a) Overtone, $2\omega_2$, and (b) combination, $2\omega_2 + \omega_3$, rovibrational transitions. The spectrum $\alpha(0)$ was measured after the temperature jump from 45 to 10 K (black), and the difference $\Delta\alpha = \alpha(0) - \alpha(\Delta t)$ was measured $\Delta t = 2.75$ h later (blue). Numbers 3–8 label the transitions shown in Fig. 1(c). The sample filling factor $f = 0.8$.

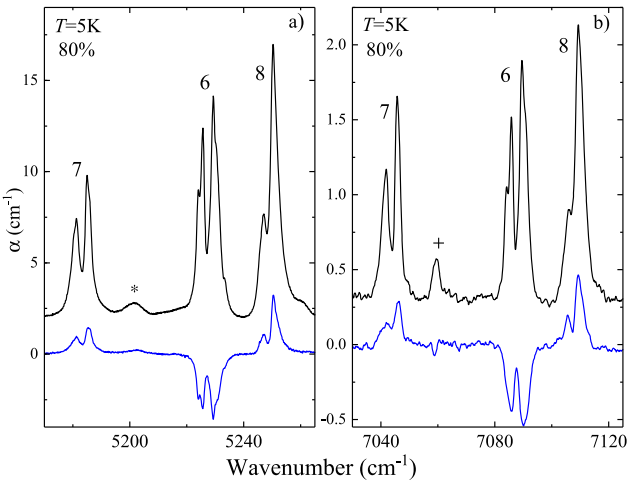

FIG. 6. Absorption spectra of $H_2O@C_{60}$ at 5 K. Rovibrational combination (a) $\omega_2 + \omega_3$ and (b) $\omega_1 + \omega_3$ transitions. The spectrum $\alpha(0)$ was measured after the temperature jump from 30 to 5 K (black), and the difference $\Delta\alpha = \alpha(0) - \alpha(\Delta t)$ was measured $\Delta t = 0.83$ h later (blue). Numbers 6–8 label the transitions shown in Fig. 1(c). (∗) in (a) at 5202 cm^{-1} marks the $\omega_2 + \omega_3$ rovibrational transition from the thermally excited rovibrational state $|000\rangle|1_{10}\rangle$ to $|011\rangle|1_{11}\rangle$. The $2\omega_1$ rovibrational transition at 7059 cm^{-1}, marked (+) in (b), is from $|000\rangle|0_{00}\rangle$ to $|200\rangle|1_{11}\rangle$. The sample filling factor $f = 0.8$.

with a strong rovibrational absorption line 6 of the ν_3 mode (Fig. 4), which probably obscures the 3683 cm^{-1} translational side peak of the ν_1 vibration.

The translational *ortho* transitions display a splitting of 2.9 cm^{-1} in the ground vibrational state; see Fig. 2(b), and 2.7 cm^{-1} in the excited vibrational state $|010\rangle$; see Fig. 4. These splittings may be attributed to the coupling between the water translation and rotation, associated with the interaction of the non-spherical rotating water molecule with the interior of the C_{60} cage. The spectral structure of this type has been analyzed in detail for the case of $H_2@C_{60}$.[8,10,12] The simplified theoretical model used here does not include translation–rotation coupling and cannot explain these splittings. A theoretical analysis of the translational peaks will be given in a later paper.

2. Vibrational and rovibrational transitions

The vibrational and rovibrational transitions are shown in Fig. 3. The three major features that distinguish the spectrum of $H_2O@C_{60}$ from the spectrum of free water are as follows.

a. Pure vibrational transitions. Absorptions corresponding to pure vibrational transitions, i.e., without simultaneous rotational excitation, are present around $\omega_1 = 3573$ cm^{-1} and $\omega_2 = 1570$ cm^{-1}. Both features are split into two components, labeled 1 and 2, identified from the difference spectra (Figs. 3 and 4) as *para* (1) and *ortho* (2) transitions.

Transition 1 is a transition from the ground vibrational state to the excited vibrational state without a change in the rotational state $|0_{00}\rangle$. Transition 2 is a vibrational excitation without a change in the rotational state $|1_{01}\rangle$. The corresponding transitions are forbidden because they violate the selection rule ΔK_a = odd and ΔK_c = odd [Eq. (27)]. As will be discussed in Sec. V E, the pure vibrational transitions 1 and 2 can be activated by the crystal electric field of solid $H_2O@C_{60}$.

The *ortho–para* splitting, i.e., the separation of lines 1 and 2, is 0.5 cm^{-1} for the ν_1 vibrational mode and 1.8 cm^{-1} for the ν_2 vibrational mode.

b. Spectral splittings. The rovibrational transitions 3–8 are split into two or more components (see Figs. 3 and 4). These splittings, as in the case of the rotational transitions, are absent for a water molecule in the gas phase. Moreover, transitions 3–5 have the same splitting pattern as the rotational transitions in the ground vibrational state, also labeled 3–5; see Fig. 2. Transitions 6 and 7 are special since they are between the $|0_{00}\rangle$ and $|1_{01}\rangle$ rotational states and, thus, reflect directly the splitting of the triply degenerate $|1_{01}\rangle$ state either in the ground vibrational state, transition 7, or in the excited vibrational state, transition 6 (Fig. 4).

We assign a weak *ortho* line at 3654 cm^{-1}, marked by * in Fig. 4, to the ν_3 rovibrational transition from the thermally excited rovibrational state $|000\rangle|1_{10}\rangle$ to $|001\rangle|1_{11}\rangle$. This assignment is further confirmed by calculating the transition frequency[39] with the parameters from Table III: $\omega_3 + E_{1_{11}} - E_{1_{10}} = \omega_3 + A_{001} + C_{001} - (A_{000} + B_{000}) = 3655\,cm^{-1}$.

c. Red shifts. The frequencies of vibrations are red-shifted relative to free H_2O. The stretching mode frequencies are red-shifted by about 2.4%, while the bending mode frequencies are red-shifted by about 1.6%; see Table II.

3. Overtone and combination rovibrational transitions

Overtone and combination vibrational transitions where two vibrational quanta are excited are presented for the $2\omega_2$

TABLE I. Rotational and rovibrational transition frequencies ω_{ji} (unit: cm^{-1}) and normalized absorption cross sections $\langle\sigma_{ji}\rangle$ (unit: cm per molecule) [Eq. (3)] from the ground *para*, $|0_{00}\rangle$, and ground *ortho*, $|1_{01}\rangle$, rotational states of $H_2O@C_{60}$ and of free H_2O. The initial vibrational state is $|000\rangle$ for all transitions. The spectral lines are labeled by Nos. 1–8, each number associated with one pair of initial and final rotational states. The frequency $\omega_{ji}^{C_{60}}$ of lines 3–8 is the intensity-weighted average of line sub-component frequencies. ω_{ji}^{gas} and $\langle\sigma_{ji}^{gas}\rangle$ are from Ref. 49. The *para*–*ortho* index k in $\langle\sigma_{ji}^{(k)}\rangle$ has been dropped to simplify the notation.

$\lvert\nu_1\nu_2\nu_3\rangle_j$	No.	$\lvert J_{K_aK_c}\rangle_i$	$\lvert J_{K_aK_c}\rangle_j$	ω_{ji}^{gas}	$\omega_{ji}^{C_{60}}$	$\langle\sigma_{ji}^{gas}\rangle$	$\langle\sigma_{ji}^{C_{60}}\rangle$	$\langle\sigma_{ji}^{gas}\rangle/\langle\sigma_{ji}^{C_{60}}\rangle$
000	3	1_{01}	1_{10}	18.6	16.8	$(3.97 \pm 0.08)10^{-17}$	$(3.24 \pm 0.26)10^{-18}$	12.1
	4	0_{00}	1_{11}	37.1	33.6	$(5.30 \pm 0.11)10^{-17}$	$(3.02 \pm 0.19)10^{-18}$	17.3
	5	1_{01}	2_{12}	55.7	51.1	$(1.191 \pm 0.024)10^{-16}$	$(7.5 \pm 0.4)10^{-18}$	16.0
100	1	0_{00}	0_{00}	3657.1	3573.2		$(3.4 \pm 0.6)10^{-20}$	
	2	1_{01}	1_{01}					
	3	1_{01}	1_{10}	3674.7	3589.1	$(5.03 \pm 0.05)10^{-19}$	$(2.89 \pm 0.03)10^{-19}$	1.74
	4	0_{00}	1_{11}	3693.3	3606.5	$(3.01 \pm 0.03)10^{-19}$	$(1.93 \pm 0.14)10^{-19}$	1.56
	5	1_{01}	2_{12}	3711.1	3623.5	$(3.97 \pm 0.04)10^{-19}$	$(1.57 \pm 0.12)10^{-19}$	2.52
010	1	0_{00}	0_{00}	1594.8	1569.3		$(2.3 \pm 0.6)10^{-19}$	
	2	1_{01}	1_{01}					
	3	1_{01}	1_{10}	1616.7	1588.5	$(1.66 \pm 0.03)10^{-17}$	$(1.03 \pm 0.11)10^{-18}$	16.1
	4	0_{00}	1_{11}	1635.0	1605.3	$(1.132 \pm 0.023)10^{-17}$	$(6.79 \pm 0.23)10^{-19}$	16.7
	5	1_{01}	2_{12}	1653.3	1623.4	$(1.73 \pm 0.04)10^{-17}$	$(1.26 \pm 0.09)10^{-18}$	13.7
001	6	0_{00}	1_{01}	3779.5	3682.1	$(8.08 \pm 0.09)10^{-18}$	$(1.73 \pm 0.21)10^{-18}$	4.66
	7	1_{01}	0_{00}	3732.1	3637.4	$(8.64 \pm 0.09)10^{-18}$	$(1.31 \pm 0.12)10^{-18}$	6.57
	8	1_{01}	2_{02}	3801.4	3703.7	$(1.526 \pm 0.015)10^{-17}$	$(2.18 \pm 0.10)10^{-18}$	6.99
011	6	0_{00}	1_{01}	5354.9	5228.0	$(8.75 \pm 0.09)10^{-19}$	$(1.15 \pm 0.06)10^{-19}$	7.63
	7	1_{01}	0_{00}	5307.5	5183.6	$(8.97 \pm 0.09)10^{-19}$	$(8.22 \pm 0.04)10^{-20}$	10.9
	8	1_{01}	2_{02}	5376.9	5249.2	$(1.703 \pm 0.017)10^{-18}$	$(1.34 \pm 0.06)10^{-19}$	12.7
101	6	0_{00}	1_{01}	7273.0	7088.4	$(5.5 \pm 0.5)10^{-19}$	$(1.261 \pm 0.021)10^{-20}$	43.4
	7	1_{01}	0_{00}	7226.0	7043.5	$(5.7 \pm 0.6)10^{-19}$	$(1.044 \pm 0.012)10^{-20}$	54.6
	8	1_{01}	2_{02}	7294.1	7109.3	$(1.07 \pm 0.11)10^{-18}$	$(1.85 \pm 0.05)10^{-20}$	57.7
020	4	0_{00}	1_{11}	3196.1	3142.0	$(7.72 \pm 0.07)10^{-20}$	$(5.5 \pm 0.4)10^{-21}$	14.1

transition in Fig. 5(a) and for the $\omega_2 + \omega_3$ and $\omega_1 + \omega_3$ transitions in Figs. 6(a) and 6(b). A three-quantum transition, $2\omega_2 + \omega_3$, is shown in Fig. 5(b). Rotational levels involved are sketched in Fig. 1(c). Again, the splitting pattern of each higher order rovibrational transition is similar to the splitting of the rotational transition with $\Delta v_i = 0$ (Fig. 2) and rovibrational transitions with $\Delta v_i = +1$ (Figs. 3 and 4).

We assign a line marked by "+" at 7059 cm^{-1} to $2\omega_1$ plus *para*-H_2O rotational transition, $0_{00} \rightarrow 1_{11}$ [Fig. 6(b)]. Another two rotational side peaks of $2\omega_1$ are *ortho* transitions 3 and 5 expected at $2\omega_1 + E_{1_{10}} - E_{1_{01}} = 7042\,cm^{-1}$ and at $2\omega_1 + E_{2_{12}} - E_{1_{01}} = 7076\,cm^{-1}$, where $E_{1_{10}} - E_{1_{01}} = A - C$ and $E_{2_{12}} - E_{1_{01}} = A + 3C$,[39] with the approximation $A = A_{200} \approx A_{100}$, $C = C_{200} \approx C_{100}$. The numerical values of A_{100} and C_{100} are taken from Table III. The first line overlaps with line 7, rovibrational transition of $\omega_1 + \omega_3$. The second line is not observed, but this could be due to the low intensity of *ortho* line 5 relative to *para* line 4; see, for example, Fig. 5(a).

All two-quantum and three-quantum vibrational transitions are red-shifted approximately by 2.4% except $2\omega_2$ where the red shift is 1.5%; see Table II.

B. Spectral fitting with a quantum mechanical model

A synthetic spectrum consisting of Gaussian lines with full width at half maximum 1.5 cm^{-1} was calculated from the experimental normalized line areas $\langle A_{ji}^{(k)}\rangle$ [Eq. (2)] using $f = 1$, $n_o = 0.7$, $n_p = 0.3$, and $T = 5$ K. The parameters of the model Hamiltonian (from Sec. III A) and the transition dipole moments (from Sec. III B) were determined with a non-linear least squares method by minimizing the difference in synthetic and modeled spectra squared, Appendix C. The reported parameter error is the average of errors calculated with $+\delta a_\nu$ and $-\delta a_\nu$ in Eq. (C9), where the parameter variation of the νth parameter at its best value $\mathbf{a}_{min}^{\nu}$ is $|\delta a_\nu| = 0.005\,\mathbf{a}_{min}^{\nu}$. The fit was applied to the rotational transitions in the ground vibrational state $|000\rangle$ and to the rovibrational transitions from the ground state to the vibrational states $|010\rangle$, $|100\rangle$, and $|001\rangle$. In total, 45 absorption lines were fitted.

The synthetic experimental spectra and the best fit spectra are shown in Fig. 7, with the best fit parameters given in Table III. The result of the fit overlaps well with the synthetic spectrum, except for transition 5 as seen in the first three panels of Fig. 7. While, for

TABLE II. Frequencies of symmetric stretching (ω_1), symmetric bending (ω_2), and asymmetric stretching (ω_3) modes and of their combinations $2\omega_2$, $\omega_2 + \omega_3$, $2\omega_2 + \omega_3$, $2\omega_1$, and $\omega_1 + \omega_3$ measured from the ground vibrational state $|000\rangle$ for $H_2O@C_{60}$ (this work) and for free H_2O.[50] *ortho* and *para* components of pure vibrational transitions v_1 and v_2 are indicated by superscripts o and p. The frequencies of transitions involving v_3 in $H_2O@C_{60}$ are the average of frequencies of transitions 6 and 7; see Figs. 4, 5(b), and 6. The overtone $2\omega_2$ is estimated from the frequency of line 4 [Fig. 5(a)], $2\omega_2 + E_{1_{11}} = 3141\ \mathrm{cm}^{-1}$, where $E_{1_{11}} = A + C$ is the energy of the rotational state $|1_{11}\rangle$,[39] in which $A = A_{010}$ and $C = C_{010}$ from Table III. The $2\omega_1$ overtone frequency is estimated from the frequency of the *para* line $2\omega_1 + E_{1_{11}} = 7059\ \mathrm{cm}^{-1}$ [Fig. 6(b)], where $E_{1_{11}} = A_{100} + C_{100}$. The shift $\Delta\omega = \omega_{C_{60}} - \omega_{\mathrm{gas}}$.

$\lvert v_1 v_2 v_3\rangle$	$H_2O@C_{60}$ cm^{-1}	Free H_2O cm^{-1}	$\Delta\omega$ cm^{-1}	$\Delta\omega/\omega_{\mathrm{gas}}$
$\lvert 010\rangle$	1569.2^{o}	1594.8	−25.6	−0.016
	1571.0^{p}			
$\lvert 100\rangle$	3573.2^{o}	3657.1	−83.9	−0.023
	3573.7^{p}			
$\lvert 001\rangle$	3659.6	3755.3	−95.7	−0.025
$\lvert 020\rangle$	3105.5	3151.6	−46.1	−0.015
$\lvert 011\rangle$	5205.2	5331.3	−126.1	−0.024
$\lvert 021\rangle$	6716.6	6871.5	−154.9	−0.023
$\lvert 200\rangle$	7027.0	7201.5	−173.5	−0.024
$\lvert 101\rangle$	7065.8	7249.8	−184.0	−0.025

other transitions, one or two Gaussian components were sufficient, the experimental transition lineshape required three components to get a reliable fit of its line area. In addition, transitions 6 and 7 were represented by two components in the synthetic spectrum, although four peaks are seen in the experimental spectrum (Fig. 4). The additional structure of experimental peaks may originate from the merohedral disorder as discussed in Sec. V E.

Tables IV and V list energies and the main components of rotational states in the ground vibrational state. The rotational energies are in qualitative agreement with recent computational estimates.[51] The $2J + 1$ degeneracy of rotational states is fully removed by the electrostatic field interacting with dipole and quadrupole moments of H_2O.

From our fit, the permanent dipole moment μ^x of the encapsulated water is given by the absorption cross section of the IR rotational transitions 3–5 in the ground vibrational state. With the value of μ^x in hand and by using the intensities of transitions 1 and 2, we were able to determine the internal static electric field in solid C_{60}. The interaction of μ^x with the crystal electric field mixes rotational states within ground and excited vibrational states. For example, in case of *ortho*-water, the components of state $|1_{10}\rangle$ are mixed into the ground state $|1_{01}\rangle$, Table V. This mixing gives the oscillator strength to the pure vibrational transitions 1 and 2. As shown in Table III, the fitted value of the electric field at the C_{60} cage centers is $(110 \pm 5)10^6\ \mathrm{V\ m}^{-1}$.

A splitting of 4 cm^{-1} is observed for transition 7 and is due to the splitting of the *ortho* ground state $|1_{01}\rangle$ [Fig. 1(c)]. In principle, a splitting could be caused by the interaction of the water electric dipole with an electric field, or by the interaction of the water electric quadrupole moment with an electric field gradient. The electric field 110×10^6 V m^{-1} is too small to cause splitting of this magnitude. This electric field lifts the degeneracy of $m = \pm 1$ levels of $|1_{01}\rangle$, but the gap between $m = 0$ and $m = \pm 1$ levels

TABLE III. Parameters obtained from the quantum mechanical model fit of IR spectra of $H_2O@C_{60}$ at $T = 5$ K (Fig. 7). The vibration frequencies ω_i, rotational constants $A_{\mathbf{v}}$, $B_{\mathbf{v}}$, $C_{\mathbf{v}}$, and quadrupolar energy $V_{\mathrm{Q}}Q_{zz}$ are in units of cm^{-1}; electric field $\mathscr{E}$ in 10^6 V m^{-1}; θ_E in radians; and dipole moment μ^x (B13) and transition dipole moments $\mu_{0i}^{x,z}$ (B14) in D. It is assumed that μ^x and Q_{zz} do not depend on the vibrational state. The parameters with zero error were not fitted.

Parameter	Value	Error
n_{o}	0.7	0
f	1	0
ω_1	3574.1	0.3
ω_2	1569.2	0.3
ω_3	3659.9	0.9
A_{000}	24.15	0.17
B_{000}	15.3	0.8
C_{000}	8.48	0.07
A_{100}	23.1	0.3
B_{100}	14.3	0.8
C_{100}	8.50	0.09
A_{010}	26.7	0.3
B_{010}	14.6	0.9
C_{010}	8.81	0.07
A_{001}	26	6
B_{001}	15	3
C_{001}	8.2	1.8
μ^x	0.474	0.008
μ_{01}^x	1.031×10^{-2}	0.021×10^{-2}
μ_{02}^x	3.40×10^{-2}	0.05×10^{-2}
μ_{03}^z	2.83×10^{-2}	0.07×10^{-2}
$\mathscr{E}$	110	5
θ_E	1.4	1.0
$V_{\mathrm{Q}}Q_{zz}$	−5.0	0.5

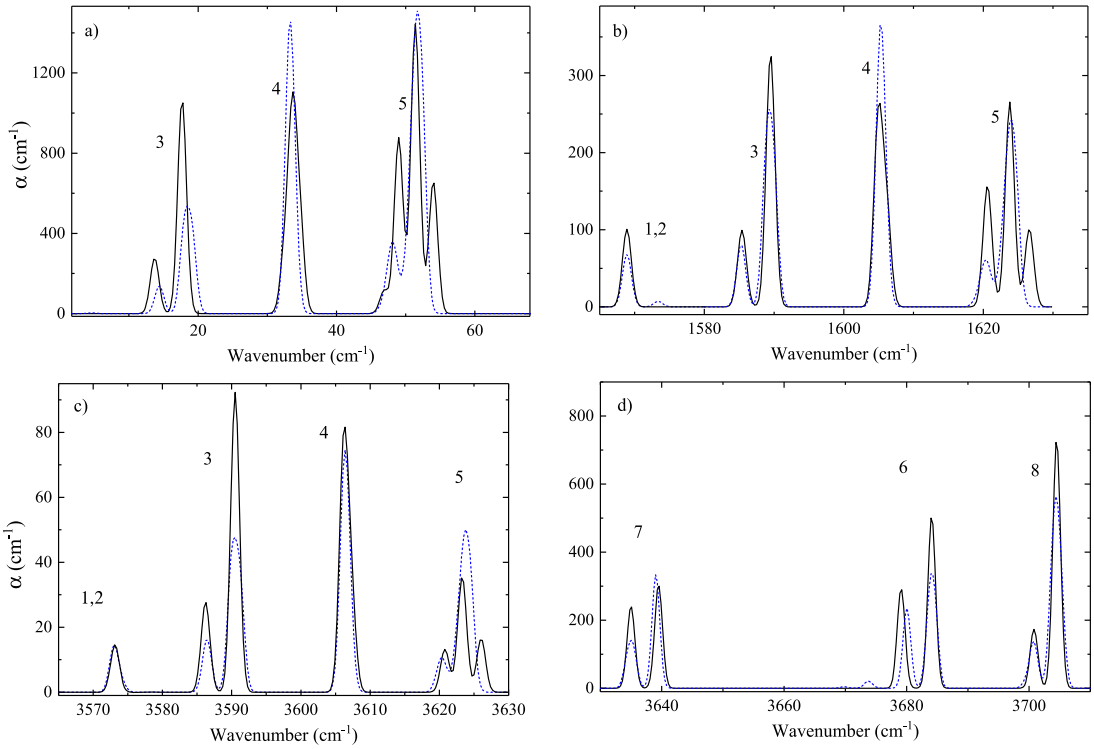

FIG. 7. Synthetic experimental spectra (black solid line) and spectra calculated with the best fit parameters from Table III (blue dashed line) with the filling factor $f = 1$ and *ortho* fraction $n_o = 0.7$ and at a temperature of 5 K. (a) Rotational transitions in the ground vibrational state. Vibrational (1 and 2) and rovibrational (3–5) transitions of (b) v_2 and (c) v_1. (d) Rovibrational transitions (6–8) of v_3.

TABLE IV. *para*-$H_2O@C_{60}$ rotational energies and wavefunctions in the ground vibrational state calculated with the best fit parameters from Table III. Wavefunction components with the absolute value of the amplitude less than 0.1 are omitted; $|J,-k,-m\rangle \equiv |J,\bar{k},\bar{m}\rangle$.

$J_{K_aK_c}$	Energy (cm^{-1})	Wavefunction in the symmetric top basis $\|J,k,m\rangle$
0_{00}	0	$-0.99\,\|0,0,0\rangle$
1_{11}	33.07	$0.49\left(\|1,\bar{1},\bar{1}\rangle + \|1,\bar{1},1\rangle - \|1,1,\bar{1}\rangle - \|1,1,1\rangle\right)$
	33.19	$-0.69\left(\|1,\bar{1},0\rangle - \|1,1,0\rangle\right)$
	33.75	$0.48\left(\|1,\bar{1},\bar{1}\rangle - \|1,\bar{1},1\rangle - \|1,1,\bar{1}\rangle + \|1,1,1\rangle\right)$
2_{02}	67.04	$-0.96\,\|2,0,0\rangle + 0.15\left(\|2,\bar{2},0\rangle + \|2,2,0\rangle\right)$
	67.73	$0.68\left(\|2,0,\bar{1}\rangle + \|2,0,1\rangle\right)$
	68.35	$0.68\left(\|2,0,\bar{1}\rangle - \|2,0,1\rangle\right)$
	71.27	$0.68\left(\|2,0,\bar{2}\rangle - \|2,0,2\rangle\right)$
	71.30	$-0.68\left(\|2,0,\bar{2}\rangle + \|2,0,2\rangle\right)$
2_{11}	94.65	$-0.4\left(\|2,\bar{1},0\rangle + \|2,1,0\rangle\right) + 0.41\left(\|2,\bar{1},\bar{2}\rangle + \|2,\bar{1},2\rangle + \|2,1,\bar{2}\rangle + \|2,1,2\rangle\right)$
	94.72	$-0.49\left(\|2,\bar{1},\bar{2}\rangle - \|2,\bar{1},2\rangle + \|2,1,\bar{2}\rangle - \|2,1,2\rangle\right)$
	94.85	$-0.53\left(\|2,\bar{1},0\rangle + \|2,1,0\rangle\right) - 0.24\left(\|2,\bar{1},\bar{2}\rangle + \|2,\bar{1},2\rangle + \|2,1,\bar{2}\rangle + \|2,1,2\rangle\right)$ $-0.21\left(-\|2,\bar{1},\bar{1}\rangle + \|2,\bar{1},1\rangle - \|2,1,\bar{1}\rangle + \|2,1,1\rangle\right)$
	94.91	$0.45\left(-\|2,\bar{1},\bar{1}\rangle + \|2,\bar{1},1\rangle - \|2,1,\bar{1}\rangle + \|2,1,1\rangle\right) - 0.21\left(\|2,\bar{1},0\rangle + \|2,1,0\rangle\right)$ $-0.15\left(\|2,\bar{1},\bar{2}\rangle + \|2,\bar{1},2\rangle + \|2,1,\bar{2}\rangle + \|2,1,2\rangle\right)$
	95.01	$0.49\left(\|2,\bar{1},\bar{1}\rangle + \|2,\bar{1},1\rangle + \|2,1,\bar{1}\rangle + \|2,1,1\rangle\right)$

TABLE V. *ortho*-$H_2O@C_{60}$ rotational energies, counted from the *para* ground state $|0_{00}\rangle$, and wavefunctions in the ground vibrational state calculated with the best fit parameters from Table III. Wavefunction components with the absolute value of the amplitude less than 0.1 are omitted; $|J,-k,-m\rangle \equiv |J,\bar{k},\bar{m}\rangle$.

$J_{K_aK_c}$	Energy (cm^{-1})	Wavefunction in the symmetric top basis $\|J,k,m\rangle$
1_{01}	20.89	$0.97\,\|1,0,0\rangle$
	24.58	$-0.69\left(\|1,0,\bar{1}\rangle+\|1,0,1\rangle\right)+0.16\left(\|1,\bar{1},0\rangle+\|1,1,0\rangle\right)$
	25.51	$-0.7\left(\|1,0,\bar{1}\rangle-\|1,0,1\rangle\right)$
1_{10}	38.88	$0.49\left(\|1,\bar{1},\bar{1}\rangle-\|1,\bar{1},1\rangle+\|1,1,\bar{1}\rangle-\|1,1,1\rangle\right)$
	40.03	$0.48\left(\|1,\bar{1},\bar{1}\rangle+\|1,\bar{1},1\rangle+\|1,1,\bar{1}\rangle+\|1,1,1\rangle\right)+0.24\|1,0,0\rangle$
	43.62	$0.69\left(\|1,\bar{1},0\rangle+\|1,1,0\rangle\right)$
2_{12}	72.29	$0.71\left(\|2,\bar{1},0\rangle-\|2,1,0\rangle\right)$
	73.12	$-0.49\left(\|2,\bar{1},\bar{1}\rangle+\|2,\bar{1},1\rangle-\|2,1,\bar{1}\rangle-\|2,1,1\rangle\right)$
	73.36	$-0.49\left(\|2,\bar{1},\bar{1}\rangle-\|2,\bar{1},1\rangle-\|2,1,\bar{1}\rangle+\|2,1,1\rangle\right)$
	75.87	$-0.49\left(\|2,\bar{1},\bar{2}\rangle-\|2,\bar{1},2\rangle-\|2,1,\bar{2}\rangle+\|2,1,2\rangle\right)$
	75.88	$-0.49\left(\|2,\bar{1},\bar{2}\rangle+\|2,\bar{1},2\rangle-\|2,1,\bar{2}\rangle-\|2,1,2\rangle\right)$
2_{21}	119.5	$-0.49\left(\|2,\bar{2},\bar{2}\rangle+\|2,\bar{2},2\rangle-\|2,2,\bar{2}\rangle-\|2,2,2\rangle\right)$
	119.5	$0.49\left(\|2,\bar{2},\bar{2}\rangle-\|2,\bar{2},2\rangle-\|2,2,\bar{2}\rangle+\|2,2,2\rangle\right)$
	122.2	$0.49\left(\|2,\bar{2},\bar{1}\rangle-\|2,\bar{2},1\rangle-\|2,2,\bar{1}\rangle+\|2,2,1\rangle\right)$
	122.2	$0.49\left(\|2,\bar{2},\bar{1}\rangle+\|2,\bar{2},1\rangle-\|2,2,\bar{1}\rangle-\|2,2,1\rangle\right)$
	123.1	$0.71\left(\|2,\bar{2},0\rangle-\|2,2,0\rangle\right)$

is due to the quadrupolar interaction. As the splitting is determined by the product of V_Q and Q_{zz}, it is not possible to have an estimate of how much is the water quadrupole moment Q_{zz} screened in C_{60}.

V. DISCUSSION

A. Vibrations of confined H_2O

All eight frequencies of the encapsulated H_2O vibrations found in this work are red-shifted relative to those of free water; see Table II. The red shift of the vibrational frequency has been observed for other endofullerenes, $H_2@C_{60}$,[10–12] HD and $D_2@C_{60}$,[8] and $HF@C_{60}$.[5] Six water modes have a relative shift between −2.3% and −2.5%. Two frequencies, namely, the bond-bending mode frequency ω_2 and its overtone frequency $2\omega_2$, are shifted by −1.6% and −1.5%, respectively.

The observed red shifts of the stretching mode frequencies ω_1 and ω_3 are only partially consistent with previous density functional theory (DFT) calculations. The DFT-based calculations published by Varadwaj *et al.*[52] do predict vibrational red shifts, while some of the calculations reported by Farimani *et al.*[53] predict blue shifts rather than red shifts.

The calculation predicts a blue shift of the bending mode ω_2 although ten times less in absolute value than the predicted shift of stretching modes.[52] The experimental shift of ω_2 is less than that of stretching modes, but it is still red-shifted. The other method, fully coupled nine-dimensional calculation, predicts blue shifts for all three vibrational modes.[51]

B. Translations of H_2O

Table VI lists the measured translational energies from the ground to the first excited state, ω_t, of small-molecule endofullerenes. It is known that the potential of di-hydrogen in C_{60} is anharmonic,[8–12] while the degree of anharmonicity of $HF@C_{60}$ and $H_2O@C_{60}$ potentials is not known. For simplicity, we assume that the potential is harmonic for the current case of endohedral molecules, $\omega_t \approx \omega_t^0$, and show its scaling relative to H_2 in Table VI. In this approximation, the harmonic potential parameter is similar among the hydrogen isotopologs, but for HF and H_2O, V_2 is larger by a factor of 1.9 and 3.4, respectively. The steeper translational potential for HF and H_2O, relative to dihydrogen, is consistent with the larger size of these molecules and, hence, their tighter confinement. The last line of Table VI is the frequency and the harmonic potential of $H_2O@C_{60}$ derived by Bacic and co-workers[16,51] using Lennard-Jones potentials. The calculated potential is steeper than the experimentally determined potential.

As seen in Fig. 2(b), the absorption line of the *ortho*-H_2O translational mode is split by 2.9 cm^{-1}. This splitting may be attributed to

TABLE VI. Translational energies from the ground to the first excited state, ω_t, of small-molecule endofullerenes and scaling of the harmonic spherical potential V_2 for the translational motion of an endohedral molecule, of mass m_i, relative to the $H_2@C_{60}$ potential $V_2^{H_2}$. The anharmonicity is neglected, $\omega_t \approx \omega_t^0$, where ω_t^0 is the frequency of an harmonic oscillator [Eq. (18)].

Molecule	m_i	ω_t (cm^{-1})	$V_2/V_2^{H_2}$	References
H_2	2	179.5	1	12
HD	3	157.7	1.16	8
D_2	4	125.9	0.98	8
HF	20	78.6	1.92	5
H_2O	18	110	3.4	This work
H_2O	18	162	7.3	Theory[16,51]

the coupling between the endohedral molecule translation and rotation, associated with the interaction of the non-spherical rotating molecule with the interior of the C_{60} cage, as seen in H_2@C_{60}.[8,10,12] For the particular transition, shown in Fig. 2(b), it is the coupling between the translational state with $N = 1$, $L = 1$ and the rotational state $|1_{01}\rangle$ of *ortho*-water. Within spherical symmetry, a good quantum number is $\Lambda = J + L$. Thus, the translation–rotation coupled translational state $L = 1$ and rotational state $J = 1$ form three states with Λ-values 0, 1, and 2. The calculated energy difference of *ortho*-water $\Lambda = 0$ and $\Lambda = 1$ states is 8 cm^{-1}[16] as compared to the experimental value 2.9 cm^{-1}.

C. Rotations of H_2O

There are two possibilities why the rotational constants of water change when it is encapsulated. The first is that the bond length and angles of H_2O change. The second is that H_2O, because of confinement and being non-centrosymmetric, is forced to rotate about the "center of interaction," which does not coincide with its nuclear center of mass.[54]

The rotational constant relates to the moment of inertia I_{aa} as $A = h(8\pi^2 c_0 I_{aa})^{-1}$, where c_0 is the speed of light. Similarly, $B = h(8\pi^2 c_0 I_{bb})^{-1}$ for the b-axis rotation and $C = h(8\pi^2 c_0 I_{cc})^{-1}$ for the c-axis rotation ($[A] = m^{-1}$ in SI units and $0.01[A] = cm^{-1}$). The moments of inertia are $I_{\alpha\alpha} = \sum_i m_i(\beta_i^2 + \gamma_i^2)$, where $\{\alpha_i, \beta_i, \gamma_i\}$ are the Cartesian coordinates of the ith nucleus with mass m_i with the origin at the nuclear center of mass.

For non-centrosymmetric molecules, the translation–rotation coupling shifts the rotational energy levels. In quantum mechanical terms, the shift of rotational states is caused by the mixing of rotational and translational states by translation–rotation coupling, for example, HD@C_{60}.[8,55] Translation–rotation coupling was not included in our quantum mechanical model of H_2O@C_{60}. The rotational constants of the model were free parameters to capture the effect of translation–rotation coupling and the change in the H_2O molecule geometry caused by the C_{60} cage. The rotational constants of free water are $A_0 = 27.88$ cm^{-1}, $B_0 = 14.52$ cm^{-1}, and $C_0 = 9.28$ cm^{-1} in the ground vibrational state.[56] The rotational constants of endohedral water have relative shifts −13%, 5.5%, −8.7% for A_0, B_0, and C_0, in the ground vibrational state, Table III. In the following discussion, we use classical arguments to assess whether the shift of rotational levels is caused by the change in water molecule geometry or by the translation–rotation coupling.

From the symmetry of the H_2O molecule, it is seen that the nuclear center of mass is on the b axis (Fig. 1). The shift of H_2O center of rotation in the negative direction of b axis decreases A and C, while it does not affect B. If B changes, it must be due to the change in H–O–H bond angle and O–H bond length. The calculation predicts the lengthening of the H–O bond by 0.0026 Å and decrease in the H–O–H bond angle by 0.87° of caged water with respect to free water.[52] With these parameters, the relative change in rotational constants A, B, and C is −2.5%, 0.65%, and −0.46%, an order of magnitude smaller than those derived from the IR spectra of H_2O@C_{60}. However, shifting the rotation center by −0.07 Å in the b direction (further away from oxygen) gives relative changes −14%, 0.65%, and −5.2%. This relative change in A_{000} and C_{000} is not very different from the values derived from the IR spectra, while the relative change in B_{000} is within the error limits, Table III. Thus, it is likely that the dominant contribution to the observed changes in rotational constants in the ground translational state comes not from the change in H_2O molecule bond lengths and bond angle but from shifting its center of rotation away from the nuclear center of mass of the H_2O molecule.

D. Permanent and transition dipole moments

A comparison of the normalized absorption cross sections $\langle\sigma_{ji}\rangle$ [Eq. (3)] for H_2O@C_{60} and for free water is given in the last column of Table I. In general, for all observed transitions, the absorption cross section of endohedral water is smaller than that of free water. The ν_1 mode has the smallest relative change, while the largest relative change is for the combination mode $\omega_1 + \omega_3$.

The comparison of H_2O@C_{60} and free H_2O absorption cross sections (Table I) enables us to estimate independently from the spectral fit the permanent and transition dipole moments of encapsulated H_2O,

$$\mu_{ji}^{C_{60}} = \mu_{ji}^{gas}\sqrt{\frac{\langle\sigma_{ji}^{C_{60}}\rangle\,\omega_{ji}^{gas}}{\langle\sigma_{ji}^{gas}\rangle\,\omega_{ji}^{C_{60}}}}. \tag{28}$$

The results are collected together with the dipole moments obtained from the fit of IR spectra in Table VII. The permanent dipole moment of encapsulated water is nearly four times smaller than that of free H_2O. The results of the IR spectroscopy study are consistent with the dipole moments determined by the capacitance method, 0.51 ± 0.05 D.[17] The reduction of the fullerene-encapsulated water dipole moment has been predicted by several theoretical calculations.[18,52,60,61]

E. Effect of solid C_{60} crystal field

The electric dipolar and quadrupolar interactions of the H_2O@C_{60} molecule with the electrostatic field in solid C_{60} explain the oscillator strength of the pure ν_1 and ν_2 vibrational transitions and the splitting of the rotational states with $J > 0$.

The theoretical work of Felker *et al.*[32] shows that the source of the quadrupole crystal field is the orientation of electron-rich double bonds of 12 nearest neighbors of C_{60} relative to the central

TABLE VII. Absolute values of the dipole moment, unit D, matrix elements of rotational [μ^x, Eq. (B13)] and rovibrational [μ_{01}^x, μ_{02}^x and μ_{03}^z, Eq. (B14)] transitions of gaseous H_2O, as published, and of H_2O@C_{60} calculated with Eq. (28) from the rotational and rovibrational absorption cross sections, Table I, and determined by the fit of IR spectra, Table III. The cross section-derived dipole moments are the cross section-error weighted averages of the three transitions, 3, 4, and 5 or 6, 7, and 8 in Table I.

	Gas	References	Cross section	Fit
μ^x	1.855	57	0.50 ± 0.05	0.474 ± 0.008
μ_{01}^x	0.0153	58	$(1.23 \pm 0.13)10^{-2}$	$(1.031 \pm 0.021)10^{-2}$
μ_{02}^x	0.1269	59	$(3.38 \pm 0.19)10^{-2}$	$(3.40 \pm 0.05)10^{-2}$
μ_{03}^z	0.0684	58	$(3.0 \pm 0.3)10^{-2}$	$(2.83 \pm 0.07)10^{-2}$

$H_2O@C_{60}$. When the solid C_{60} is cooled below 90 K, a merohedral disorder is frozen where ~85% of C_{60} have the electron-rich 6:6 bond (bond between the two hexagonal rings) facing pentagonal rings of a neighboring cage, the P-orientation.[62] The rest are H-oriented where the 6:6 bond faces neighboring cage's hexagonal rings. The calculated quadrupolar interaction for the P-oriented molecules is ten times bigger than that for the H-oriented molecules.[32] The electric field gradient couples to the quadrupole moment of water and splits the $|1_{01}\rangle$ rotational state by 4.2 cm^{-1}, where the $m = \pm 1$ doublet is above the $m = 0$ level.[32] This theoretically predicted splitting of the $|1_{01}\rangle$ state for the P-oriented molecules is remarkably close to the observed experimental value, seen as a 4 cm^{-1} splitting of line 7, transition starting from the *ortho* ground state (Fig. 4). It is not possible to determine the crystal electric field gradient tensor and the encapsulated water quadrupole moment separately from our IR spectra.

Further splitting is possible if the symmetry is lower than S_6, but the maximum number of components for $J = 1$ remains three. However, we see that line 7 consists of four components instead of three (Fig. 4). This suggests that there are two sites with different local electrostatic fields. Anomalous splitting of triply degenerate phonons into quartets has been seen in solid C_{60} by IR spectroscopy[34] and was attributed to the merohedral disorder. Thus, our work and the IR study of phonons[34] clearly show that there are two different quadrupolar interactions in solid C_{60}. As was proposed by Felker *et al.*,[32] the crystal field has a different magnitude for P-oriented sites and for H-oriented sites. The small population of H-oriented sites (about 15%) justifies our spectral fitting with a single quadrupolar interaction.

We assumed that there is an internal electric field in C_{60}, and this field is a possible reason why the pure vibrational transitions 1 and 2 [see Fig. 1(c)] become visible in the IR spectrum. It is also plausible that 1 and 2 gain intensity through the translation–rotation coupling from the induced dipole moment of translational motion. However, there is evidence that local electric fields exist in solid C_{60} as a result of merohedral disorder C_{60}.[35] The estimate of unbalanced charge by Alers *et al.*[35] was $q = 6 \times 10^{-3} e$ assuming a dipole moment $\mu = qd_0$, where e is the electron charge and $d_0 = 0.7$ nm is the diameter of a C_{60} molecule. Our estimate is that the electric field $\mathscr{E} = 1.1 \times 10^8$ V m^{-1} at the center of the C_{60} cage is created by the dipole moment with charge $q = 4.7 \times 10^{-3} e$. These two estimates are very close.

C_{60} has six nearest-neighbor equatorial cages and three axial cages above and three axial cages below the equatorial plane, following the notation of Ref. 32. The z' axis of the crystal field coordinate frame is normal to the equatorial plane. As our fit shows, the electric field is rotated away from the z' axis by $\theta_E \approx 80°$, Table III, almost into the equatorial plane. It is possible that one of the six nearest-neighbors in the equatorial plane does not have P-orientation and this mis-oriented cage is the source of the electric field. θ_E has a large relative error consistent with the probability to have the mis-oriented cage in the equatorial or in the axial position.

VI. SUMMARY

The infrared absorption spectra of solid $H_2O@C_{60}$ samples were measured close to liquid He temperature, and rotational, vibrational, rovibrational, overtone, and combination rovibrational transitions of H_2O were seen. The spectral lines were identified as *para*-water and *ortho*-water transitions by following the *para–ortho* conversion process over the timescale of hours. The vibrational frequencies are shifted by −2.4% relative to free water, except bending mode frequency ω_2 and its overtone $2\omega_2$, where the shift is −1.6%. An absorption mode due to the quantized center-of-mass motion of H_2O in the molecular cage of C_{60} was observed at 110 cm^{-1}. The dipole moment of encapsulated water is 0.50 ± 0.05 D, which is approximately four times less than that of free water and agrees with previous estimates.[17]

The rotational and rovibrational spectra were fitted with a quantum mechanical model of a vibrating rotor in the electrostatic field with dipolar and quadrupolar interactions. The quadrupolar interaction splits the $J \geq 1$ rotational states of H_2O. The source of quadrupolar interaction is the relative orientation of electron-rich chemical bonds relative to pentagonal and hexagonal motifs of C_{60} and its 12 nearest neighbors.[32] Further IR study by using pressure to change the ratio of P-oriented and H-oriented motifs[63] would provide more information on the quadrupolar crystal fields of these motifs. The finite oscillator strength of the fundamental vibrational transitions is attributed to a finite electric field at the centers of C_{60} cages due to merohedral disorder, as has been postulated in different contexts.[35] Our results are consistent with an internal electric field of 10^8 V m^{-1}. However, it is also plausible that the fundamental vibrational transitions gain intensity through the translation–rotation coupling from the dipole moment induced by the translational motion, something that can be addressed in further theoretical studies.

To conclude, H_2O in the molecular cavity of C_{60} behaves as a vibrating asymmetric top, its dipole moment is reduced, and the translational motion is quantized. The splitting of rotational levels is caused by the quadrupolar interaction with the crystal field of solid C_{60}. Evidence is found for the existence of a finite electric field at the centers of C_{60} cages in water-endofullerene due to merohedral disorder.

Two out of three components necessary for a rigorous, comprehensive description of the water translations, rotations, and vibrations inside the C_{60} molecular cage are now in place: first, the infrared spectroscopy data reported here and, second, the nine-dimensional quantum bound-state methodology[51] plus the theory of symmetry breaking in solid C_{60}.[32,33] What is missing is a high-quality *ab initio* nine-dimensional potential energy surface for this system.

ACKNOWLEDGMENTS

We thank Professor Zlatko Bačić for useful discussions. This research was supported by the Estonian Ministry of Education and Research through institutional research funding under Grant No. IUT23-3 and personal research funding under Grant No. PRG736 and the European Regional Development Fund under Project No. TK134. We acknowledge the EPSRC (UK) for support under Grant Nos. EP/P009980/1 and EP/T004320/1.

APPENDIX A: INTERACTION OF DIPOLE MOMENT WITH LOCAL ELECTRIC FIELD

The dipole moment in spherical components is[40]

$$\begin{aligned}\mu_{+1} &= -\frac{1}{\sqrt{2}}(\mu_x + i\mu_y),\\ \mu_{-1} &= \frac{1}{\sqrt{2}}(\mu_x - i\mu_y),\\ \mu_0 &= \mu_z.\end{aligned} \tag{A1}$$

The dipole moment of water in the Cartesian molecule coordinate frame, as shown in Fig. 1, is $\boldsymbol{\mu}^M = \{-\mu_x, 0, 0\}$, where we use a convention that the dipole moment is directed from the negative charge to the positive charge. Then, from Eq. (A1), the dipole moment in spherical components is

$$\{\mu^M_m\} = \frac{\mu_x}{\sqrt{2}}\{-1, 0, 1\}, \quad m = -1, 0, +1. \tag{A2}$$

We consider the coupling of the H_2O dipole moment to the local electric field, $\mathscr{E}$, with spherical coordinates $\{\mathscr{E}, \phi_E, \theta_E\}$ in the crystal frame C (frame where the electric field gradient tensor is defined) and in the coordinate frame E of electric field $\{E^E_m\} = \mathscr{E}\{0, 1, 0\}$, i.e., along the z_E axis. Corresponding Euler angles are $\Omega_{C\to E} = \{\phi_E, \theta_E, 0\}$ and $\Omega_{E\to C} = \{\pi, \theta_E, -\pi - \phi_E\}$. The dipole moment of the molecule in frame E is

$$\mu^E_m = \sum_{m'=-1}^{1} \left[D^1_{mm'}(\Omega_{E\to C})\right]^* \mu^C_{m'}. \tag{A3}$$

Here, we used Wigner D-functions relating the components of a spherical rank j irreducible tensor T_{jm} in coordinate frames A and B,[39]

$$T^B_{jm} = \sum_{m'=-j}^{j} D^j_{m'm}(\Omega_{A\to B}) T^A_{jm'} \tag{A4}$$

and

$$T^A_{jm} = \sum_{m'=-j}^{j} \left[D^j_{mm'}(\Omega_{A\to B})\right]^* T^B_{jm'}, \tag{A5}$$

where $\Omega_{A\to B} = \{\phi, \theta, \chi\}$ are Euler angles transforming coordinate frame A into frame B. The angles for the inverse transformation are $\Omega_{B\to A} = \{\pi - \chi, \theta, -\pi - \phi\}$.[41]

The interaction of the molecular dipole moment μ^M_m with the electric field is

$$\begin{aligned}\mathscr{H}_{\rm ed} &= -\sum_{m=-1}^{1} (-1)^m \mathscr{E}^E_{-m}\mu^E_m\\ &= -\sum_{m=-1}^{1} (-1)^m \mathscr{E}^E_{-m}\left[\sum_{m'=-1}^{1}\left[D^1_{mm'}(\Omega_{E\to C})\right]^*\mu^C_{m'}\right]\\ &= -\sum_{m,m'=-1}^{1} (-1)^m \mathscr{E}^E_{-m}\left[D^1_{mm'}(\Omega_{E\to C})\right]^*\mu^C_{m'}\\ &= -\sum_{m,m'=-1}^{1} (-1)^m \mathscr{E}^E_{-m}\left[D^1_{mm'}(\Omega_{E\to C})\right]^*\\ &\quad\times\left[\sum_{m''=-1}^{1}\left[D^1_{m'm''}(\Omega_{C\to M})\right]^*\mu^M_{m''}\right].\end{aligned}$$

The minus sign in front of sum in the formula above is consistent with $\mathscr{H}_{\rm ed} = -\mathscr{E}\cdot\mu$ if the spherical components of vectors $\mathscr{E}$ and μ are defined as in (A1).

APPENDIX B: INTERACTION OF DIPOLE MOMENT WITH ELECTRIC FIELD OF RADIATION

Here, we derive the electric dipole transition matrix elements of a molecule, part (21) of the absorption cross section (20). The derivation of (21) starts from

$$S_{fi} = \frac{1}{e^2}|\langle f|\mathscr{H}_{\rm ed}|i\rangle|^2, \tag{B1}$$

where

$$\mathscr{H}_{\rm ed} = -\sum_{m=-1}^{1} (-1)^m e^A_{-m}\mu^A_m, \tag{B2}$$

where the electric field of radiation, $\mathbf{e} = \{e^A_m\}$, and the dipole moment of a molecule, μ^A_m, are in the space-fixed frame A; $e^2 = \sum_{m=-1}^{1}(e^A_m)^2$.

The Euler angles of transformation of the crystal frame C to the space-fixed frame A, and vice versa, are $\Omega_{C\to A} = \{\phi_R, \theta_R, 0\}$ and $\Omega_{A\to C} = \{\pi, \theta_R, -\pi - \phi_R\}$.

The dipole moment in frame A is

$$\mu^A_m = \sum_{m'=-1}^{1}\left[D^1_{mm'}(\Omega_{A\to C})\right]^*\mu^C_{m'}, \tag{B3}$$

where μ^C_m is the dipole moment in the crystal frame C.

The absolute value of matrix element squared is

$$\begin{aligned}S_{fi} &= e^{-2}\left|\langle j|\sum_{m=-1}^{1}(-1)^m e^A_{-m}\mu^A_m|i\rangle\right|^2\\ &= e^{-2}\left|\sum_{m,m'=-1}^{1}(-1)^m e^A_{-m}\left[D^1_{mm'}(\Omega_{A\to C})\right]^*\langle j|\mu^C_{m'}|i\rangle\right|^2\\ &= e^{-2}\sum_{m_1,m_1',m_2,m_2'=-1}^{1}(-1)^{m_1+m_2}e^A_{-m_1}\left[e^A_{-m_2}\right]^*\\ &\quad\times\left[D^1_{m_1m_1'}(\Omega_{A\to C})\right]^* D^1_{m_2m_2'}(\Omega_{A\to C})\\ &\quad\times\langle j|\mu^C_{m_1'}|i\rangle\langle j|\mu^C_{m_2'}|i\rangle^*.\end{aligned} \tag{B4}$$

1. Random orientation of crystals

We assume that all the crystals are identical and there are no other static fields outside the crystal that could break the directional isotropy. We average (B4) over the random orientation of crystal coordinate frames with respect to the space-fixed frame, $\Omega_{A\to C}$, and get

$$\begin{aligned}\left\langle S_{fi}\right\rangle_{\Omega_{A\to C}} &= \frac{1}{3e^2}\sum_{m,m'=-1}^{1}\left|e^A_{-m}\right|^2\left|\langle j|\mu^C_{m'}|i\rangle\right|^2\\ &= \frac{1}{3e^2}\left(\sum_{m=-1}^{1}\left|e^A_{-m}\right|^2\right)\left(\sum_{m'=-1}^{1}\left|\langle j|\mu^C_{m'}|i\rangle\right|^2\right)\\ &= \frac{1}{3}\left(\sum_{m'=-1}^{1}\left|\langle j|\mu^C_{m'}|i\rangle\right|^2\right),\end{aligned} \tag{B5}$$

where we used the property of rotation matrices,[39]

$$\int \left[D^{j_1}_{m_1 m_1'}(\Omega)\right]^* D^{j_2}_{m_2 m_2'}(\Omega)\mathrm{d}\Omega = \frac{8\pi^2}{2j_1+1}\delta_{j_1 j_2}\delta_{m_1 m_2}\delta_{m_1' m_2'} \tag{B6}$$

and

$$\int_0^{\pi} \sin\theta_R \mathrm{d}\theta_R \int_0^{2\pi} \mathrm{d}\phi_R \int_0^{2\pi} \mathrm{d}\chi_R = 8\pi^2. \tag{B7}$$

If the sample is in the powder form, then it follows from Eq. (B5) that the absorption is independent of light polarization.

2. Transition matrix element and separation of coordinates

The absorption of radiation by a molecule [Eq. (20)] depends on the matrix elements of an electric dipole moment between the initial and final states,

$$\sum_{\sigma=-1}^{1} \left|\left\langle \Phi' \middle| \mu_\sigma^A \middle| \Phi \right\rangle\right|^2, \tag{B8}$$

where μ_σ^A is the molecule dipole moment in the space-fixed coordinate frame. The molecule wavefunction consists of the nuclear spin wavefunction $|Im_I\rangle$, electron wavefunction $|\Phi^e\rangle$, electron spin wavefunction $|Sm_S\rangle$, vibration wavefunction $|\Phi^v\rangle$, and rotation wavefunction $|\Phi^r\rangle$,[40]

$$|\Phi\rangle = |Im_I\rangle|Sm_S\rangle\left|\Phi^e\Phi^v\Phi^r\right\rangle. \tag{B9}$$

Using these separable wavefunctions, the matrix element (B8) is[40]

$$\left\langle \Phi' \middle| \mu_\sigma^A \middle| \Phi \right\rangle = \left\langle I' m_I' \middle| Im_I \right\rangle \left\langle S' m_S' \middle| Sm_S \right\rangle \times \sum_{\sigma'=-1}^{1} \left\langle \Phi^{r'} \middle| D^1_{\sigma\sigma'}(\Omega_{A\to M})^* \middle| \Phi^r \right\rangle \left\langle \Phi^{v'} \middle| \mu_{\sigma'}^{M(e)} \middle| \Phi^v \right\rangle, \tag{B10}$$

where

$$\mu_\sigma^{M(\mathrm{e})} = \left\langle \Phi^{e'} \middle| \mu_\sigma^M \middle| \Phi^e \right\rangle, \tag{B11}$$

and we have taken into account that the electric dipole moment does not depend on nuclear and electron spin coordinates. Furthermore, if the energies of initial and final states of the transition are independent of spin projections m_I and m_s, the summation over initial and final states in the transition probability leads to degeneracy factors $g_I = 2I + 1$ and $g_S = 2S + 1$ in (20). The electron spin is zero in the ground electronic state of H_2O, and thus, $g_S = 1$. Degeneracy of *para* molecules ($I = 0$) is $g_I^{(\mathrm{p})} = 1$, and that of *ortho* molecules ($I = 1$) is $g_I^{(\mathrm{o})} = 3$.

If the electronic orbital does not change in the transition, then (B8) is the molecule electric dipole moment in the ground electronic state $|\Phi^e\rangle$,

$$\mu_\sigma^{M(\mathrm{eg})} \equiv \left\langle \Phi^e \middle| \mu_\sigma^M \middle| \Phi^e \right\rangle. \tag{B12}$$

For the rest of the discussion, we use a shorthand notation μ_σ^M for the molecule dipole moment in the ground electronic state, $\mu_\sigma^{M(\mathrm{eg})}$.

Using Cartesian coordinates, the dipole moment in the ground vibrational state is

$$\mu^x = \langle 000|\mu_x^M|000\rangle. \tag{B13}$$

In the quantum mechanical model of $H_2O@C_{60}$ that we used to fit the IR spectra, we set the dipole moment equal to μ^x in three excited vibrational states $|100\rangle$, $|010\rangle$, and $|001\rangle$.

The vibrational transition dipole moments are

$$\begin{aligned} \mu_{01}^x &= \langle 100|\mu_x^M|000\rangle, \\ \mu_{02}^x &= \langle 010|\mu_x^M|000\rangle, \\ \mu_{03}^z &= \langle 001|\mu_z^M|000\rangle. \end{aligned} \tag{B14}$$

The relation between spherical and Cartesian dipole moment components is given by Eq. (A1).

APPENDIX C: FITTING OF SYNTHETIC SPECTRA WITH QUANTUM MECHANICAL MODEL AND MODEL PARAMETER ERROR ESTIMATION

We determined the Hamiltonian parameters and the dipole moments, parameter set $\mathbf{a} = \{a_1, \ldots, a_\nu, \ldots, a_M\}$, by finding the parameter set $\mathbf{a}_{\min}$ that gives the minimum value, $\chi^2_{\min}$, of function

$$\chi^2 = \sum_{i=1}^{N} [S(\nu_i) - f(\nu_i; \mathbf{a})]^2, \tag{C1}$$

where $S(\nu_i)$ is the synthetic spectrum, with argument frequency ν_i, generated from the fit of the experimental spectra and $f(\nu_i; \mathbf{a})$ is the spectrum calculated from the model with M parameters $\mathbf{a} = \{a_1, \ldots, a_\nu, \ldots, a_M\}$; N is the number of points in the spectrum. The goal is to minimize χ^2 over the parameter set $\mathbf{a}$. The result is $\chi^2_{\min}$ and $\mathbf{a}_{\min}$.

Let us define the matrix

$$F_{i\nu} = \frac{\partial f(\nu_i; \mathbf{a})}{\partial a_\nu} \tag{C2}$$

and the dispersion matrix $\bar{\boldsymbol{V}}$ [Eq. (12) of Ref. 64],

$$V_{\mu\nu} = \sum_{i=1}^{N} F_{\mu i}^T F_{i\nu}. \tag{C3}$$

The covariance matrix [Eq. (11) of Ref. 64]

$$\bar{\boldsymbol{\Theta}} = \sigma^2 \bar{\boldsymbol{V}}^{-1}, \tag{C4}$$

where $\sigma^2 = \chi^2_{min}/(N - M)$ and $\bar{\boldsymbol{V}}^{-1}$ is the inverse matrix of $\bar{\boldsymbol{V}}$, $\bar{\boldsymbol{V}}^{-1}\bar{\boldsymbol{V}} = \bar{\mathbf{1}}$.

The estimated variance of parameter a_ν is

$$\Delta a_\nu = \sqrt{\Theta_{\nu\nu}} = \sqrt{\frac{\chi^2_{\min}(\bar{\boldsymbol{V}}^{-1})_{\nu\nu}}{N - M}}. \tag{C5}$$

The correlation matrix $\bar{\boldsymbol{C}}$ is

$$C_{\nu\mu} = \frac{\Theta_{\nu\mu}}{\sqrt{\Theta_{\nu\nu}\Theta_{\mu\mu}}}. \tag{C6}$$

The element of $\bar{\boldsymbol{F}}$ [Eq. (C2)] is

$$F_{i\nu} = \frac{f(\nu_i; \mathbf{a}_{\min} + \delta a_\nu) - f(\nu_i; \mathbf{a}_{\min})}{\delta a_\nu}, \tag{C7}$$

where $\mathbf{a}_{min}$ minimizes χ^2 and δa_ν is a small variation of the parameter a_ν.

We change the sum for an integral over ν in (C1),

$$\chi^2 = \sum_k \int_{\nu_{k1}}^{\nu_{k2}} A_k^2 [S(\nu) - f(\nu; \mathbf{a})]^2 \mathrm{d}\nu, \tag{C8}$$

where the experimental spectrum is available in several spectral ranges $\{\nu_{k1}, \nu_{k2}\}$ indexed by k. A_k is the weight factor for each spectral range k. A_k is chosen so that the strongest lines for each range k are equal. The spectrum $S(\nu)$ is calculated with constant linewidth using line areas and frequencies from the fits of the experimental spectra.

By inserting (C7) into (C3) and using the continuum limit, we get the matrix $\bar{V}$,

$$\begin{aligned} V_{\mu\nu} = \frac{1}{\delta a_\mu \delta a_\nu} \sum_k A_k^2 \int_{\nu_{k1}}^{\nu_{k2}} \mathrm{d}\nu \\ \times \big[f(\nu; \mathbf{a}_{\min} + \delta a_\mu) f(\nu; \mathbf{a}_{\min} + \delta a_\nu) \\ - f(\nu; \mathbf{a}_{\min} + \delta a_\mu) f(\nu; \mathbf{a}_{\min}) \\ - f(\nu; \mathbf{a}_{\min}) f(\nu; \mathbf{a}_{\min} + \delta a_\nu) \\ + f(\nu; \mathbf{a}_{\min})^2 \big]. \end{aligned} \tag{C9}$$

We define the number of experimental points N as the number of lines fitted in the experimental spectra multiplied by two as each line has two parameters, area and frequency. We estimate the parameter error with Eq. (C5) using (C8) and (C9).

DATA AVAILABILITY

The data that support the findings of this study are available from the corresponding author upon reasonable request.

REFERENCES

[1] Y. Morinaka, F. Tanabe, M. Murata, Y. Murata, and K. Komatsu, "Rational synthesis, enrichment, and ^{13}C NMR spectra of endohedral C_{60} and C_{70} encapsulating a helium atom," Chem. Commun. **46**, 4532–4534 (2010).

[2] S. Bloodworth, G. Hoffman, M. C. Walkey, G. R. Bacanu, J. M. Herniman, M. H. Levitt, and R. J. Whitby, "Synthesis of Ar@C_{60} using molecular surgery," Chem. Commun. **56**, 10521–10524 (2020).

[3] K. Komatsu, M. Murata, and Y. Murata, "Encapsulation of molecular hydrogen in fullerene C_{60} by organic synthesis," Science **307**, 238–240 (2005).

[4] K. Kurotobi and Y. Murata, "A single molecule of water encapsulated in fullerene C_{60}," Science **333**, 613–616 (2011).

[5] A. Krachmalnicoff, R. Bounds, S. Mamone, S. Alom, M. Concistrè, B. Meier, K. Kouřil, M. E. Light, M. R. Johnson, S. Rols, A. J. Horsewill, A. Shugai, U. Nagel, T. Rõõm, M. Carravetta, M. H. Levitt, and R. J. Whitby, "The dipolar endofullerene HF@C_{60}," Nat. Chem. **8**, 953–957 (2016).

[6] S. Bloodworth, G. Sitinova, S. Alom, S. Vidal, G. R. Bacanu, S. J. Elliott, M. E. Light, J. M. Herniman, G. J. Langley, M. H. Levitt, and R. J. Whitby, "First synthesis and characterization of CH_4@C_{60}," Angew. Chem., Int. Ed. **58**, 5038 (2019).

[7] A. J. Horsewill, S. Rols, M. R. Johnson, Y. Murata, M. Murata, K. Komatsu, M. Carravetta, S. Mamone, M. H. Levitt, J. Y.-C. Chen, J. A. Johnson, X. Lei, and N. J. Turro, "Inelastic neutron scattering of a quantum translator-rotator encapsulated in a closed fullerene cage: Isotope effects and translation-rotation coupling in H_2@C_{60} and HD@C_{60}," Phys. Rev. B **82**, 081410 (2010).

[8] M. Ge, U. Nagel, D. Hüvonen, T. Rõõm, S. Mamone, M. H. Levitt, M. Carravetta, Y. Murata, K. Komatsu, X. Lei, and N. J. Turro, "Infrared spectroscopy of endohedral HD and D_2 in C_{60}," J. Chem. Phys. **135**, 114511 (2011).

[9] A. Krachmalnicoff, M. H. Levitt, and R. J. Whitby, "An optimised scalable synthesis of H_2O@C_{60} and a new synthesis of H_2@C_{60}," Chem. Commun. **50**, 13037–13040 (2014).

[10] S. Mamone, M. Ge, D. Hüvonen, U. Nagel, A. Danquigny, F. Cuda, M. C. Grossel, Y. Murata, K. Komatsu, M. H. Levitt, T. Rõõm, and M. Carravetta, "Rotor in a cage: Infrared spectroscopy of an endohedral hydrogen-fullerene complex," J. Chem. Phys. **130**, 081103 (2009).

[11] C. Beduz, M. Carravetta, J. Y. C. Chen, M. Concistré, M. Denning, M. Frunzi, A. J. Horsewill, O. G. Johannessen, R. Lawler, X. Lei, M. H. Levitt, Y. Li, S. Mamone, Y. Murata, U. Nagel, T. Nishida, J. Ollivier, S. Rols, T. Rõõm, R. Sarkar, N. J. Turro, and Y. Yang, "Quantum rotation of *ortho* and *para*-water encapsulated in a fullerene cage," Proc. Natl. Acad. Sci. U. S. A. **109**, 12894–12898 (2012).

[12] M. Ge, U. Nagel, D. Hüvonen, T. Rõõm, S. Mamone, M. H. Levitt, M. Carravetta, Y. Murata, K. Komatsu, J. Y.-C. Chen, and N. J. Turro, "Interaction potential and infrared absorption of endohedral H_2 in C_{60}," J. Chem. Phys. **134**, 054507 (2011).

[13] A. J. Horsewill, K. S. Panesar, S. Rols, J. Ollivier, M. R. Johnson, M. Carravetta, S. Mamone, M. H. Levitt, Y. Murata, K. Komatsu, J. Y.-C. Chen, J. A. Johnson, X. Lei, and N. J. Turro, "Inelastic neutron scattering investigations of the quantum molecular dynamics of a H_2 molecule entrapped inside a fullerene cage," Phys. Rev. B **85**, 205440 (2012).

[14] M. Xu, F. Sebastianelli, B. R. Gibbons, Z. Bačić, R. Lawler, and N. J. Turro, "Coupled translation-rotation eigenstates of H_2 in C_{60} and C_{70} on the spectroscopically optimized interaction potential: Effects of cage anisotropy on the energy level structure and assignments," J. Chem. Phys. **130**, 224306 (2009).

[15] M. Xu, F. Sebastianelli, Z. Bačić, R. Lawler, and N. J. Turro, "Quantum dynamics of coupled translational and rotational motions of H_2 inside C_{60}," J. Chem. Phys. **128**, 011101 (2008).

[16] P. M. Felker and Z. Bačić, "Communication: Quantum six-dimensional calculations of the coupled translation-rotation eigenstates of H_2O@C_{60}," J. Chem. Phys. **144**, 201101 (2016).

[17] B. Meier, S. Mamone, M. Concistrè, J. Alonso-Valdesueiro, A. Krachmalnicoff, R. J. Whitby, and M. H. Levitt, "Electrical detection of *ortho–para* conversion in fullerene-encapsulated water," Nat. Commun. **6**, 8112 (2015).

[18] B. Ensing, F. Costanzo, and P. L. Silvestrelli, "On the polarity of buckminsterfullerene with a water molecule inside," J. Phys. Chem. A **116**, 12184–12188 (2012).

[19] J. Ceponkus, P. Uvdal, and B. Nelander, "The coupling between translation and rotation for monomeric water in noble gas matrices," J. Chem. Phys. **138**, 244305 (2013).

[20] M. E. Fajardo, S. Tam, and M. E. DeRose, "Matrix isolation spectroscopy of H_2O, D_2O, and HDO in solid parahydrogen," J. Mol. Struct. **695-696**, 111–127 (2004), Winnewisser Special Issue.

[21] C. M. Lindsay, G. E. Douberly, and R. E. Miller, "Rotational and vibrational dynamics of H_2O and HDO in helium nanodroplets," J. Mol. Struct. **786**, 96–104 (2006).

[22] K. E. Kuyanov, M. N. Slipchenko, and A. F. Vilesov, "Spectra of the ν_1 and ν_3 bands of water molecules in helium droplets," Chem. Phys. Lett. **427**, 5–9 (2006).

[23] B. P. Gorshunov, E. S. Zhukova, V. I. Torgashev, V. V. Lebedev, G. S. Shakurov, R. K. Kremer, E. V. Pestrjakov, V. G. Thomas, D. A. Fursenko, and M. Dressel, "Quantum behavior of water molecules confined to nanocavities in gemstones," J. Phys. Chem. Lett. **4**, 2015–2020 (2013).

[24] E. S. Zhukova, V. I. Torgashev, B. P. Gorshunov, V. V. Lebedev, G. S. Shakurov, R. K. Kremer, E. V. Pestrjakov, V. G. Thomas, D. A. Fursenko, A. S. Prokhorov, and M. Dressel, "Vibrational states of a water molecule in a nano-cavity of beryl crystal lattice," J. Chem. Phys. **140**, 224317 (2014).

[25] A. I. Kolesnikov, G. F. Reiter, N. Choudhury, T. R. Prisk, E. Mamontov, A. Podlesnyak, G. Ehlers, A. G. Seel, D. J. Wesolowski, and L. M. Anovitz, "Quantum tunneling of water in beryl: A new state of the water molecule," Phys. Rev. Lett. **116**, 167802 (2016).

[26] M. A. Belyanchikov, M. Savinov, Z. V. Bedran, P. Bednyakov, P. Proschek, J. Prokleska, V. A. Abalmasov, J. Petzelt, E. S. Zhukova, V. G. Thomas, A. Dudka, A. Zhugayevych, A. S. Prokhorov, V. B. Anzin, R. K. Kremer, J. K. H. Fischer, P. Lunkenheimer, A. Loidl, E. Uykur, M. Dressel, and B. Gorshunov, "Dielectric ordering of water molecules arranged in a dipolar lattice," Nat. Commun. **11**, 3927 (2020).

[27]S. Mamone, J. Y.-C. Chen, R. Bhattacharyya, M. H. Levitt, R. G. Lawler, A. J. Horsewill, T. Rõõm, Z. Bačić, and N. J. Turro, "Theory and spectroscopy of an incarcerated quantum rotor: The infrared spectroscopy, inelastic neutron scattering and nuclear magnetic resonance of H_2@C_{60} at cryogenic temperature," Coord. Chem. Rev. **255**, 938–948 (2011).
[28]B. Meier, K. Kouřil, C. Bengs, H. Kouřilová, T. C. Barker, S. J. Elliott, S. Alom, R. J. Whitby, and M. H. Levitt, "Spin-isomer conversion of water at room temperature and quantum-rotor-induced nuclear polarization in the water-endofullerene H_2O@C_{60}," Phys. Rev. Lett. **120**, 266001 (2018).
[29]Y. Li, J. Y.-C. Chen, X. Lei, R. G. Lawler, Y. Murata, K. Komatsu, and N. J. Turro, "Comparison of nuclear spin relaxation of H_2O@C_{60} and H_2@C_{60} and their nitroxide derivatives," J. Phys. Chem. Lett. **3**, 1165–1168 (2012).
[30]S. S. Zhukov, V. Balos, G. Hoffman, S. Alom, M. Belyanchikov, M. Nebioglu, S. Roh, A. Pronin, G. R. Bacanu, P. Abramov, M. Wolf, M. Dressel, M. H. Levitt, R. J. Whitby, B. Gorshunov, and M. Sajadi, "Rotational coherence of encapsulated ortho and para water in fullerene-C_{60} revealed by time-domain terahertz spectroscopy," Sci. Rep. **10**, 18329 (2020).
[31]K. S. K. Goh, M. Jiménez-Ruiz, M. R. Johnson, S. Rols, J. Ollivier, M. S. Denning, S. Mamone, M. H. Levitt, X. Lei, Y. Li, N. J. Turro, Y. Murata, and A. J. Horsewill, "Symmetry-breaking in the endofullerene H_2O@C_{60} revealed in the quantum dynamics of *ortho* and *para*-water: A neutron scattering investigation," Phys. Chem. Chem. Phys. **16**, 21330–21339 (2014).
[32]P. M. Felker, V. Vlček, I. Hietanen, S. FitzGerald, D. Neuhauser, and Z. Bačić, "Explaining the symmetry breaking observed in the endofullerenes H_2@C_{60}, HF@C_{60}, and H_2O@C_{60}," Phys. Chem. Chem. Phys. **19**, 31274–31283 (2017).
[33]Z. Bačić, V. Vlček, D. Neuhauser, and P. M. Felker, "Effects of symmetry breaking on the translation-rotation eigenstates of H_2, HF, and H_2O inside the fullerene C_{60}," Discuss. Faraday Soc. **212**, 547–567 (2018).
[34]C. C. Homes, P. J. Horoyski, M. L. W. Thewalt, and B. P. Clayman, "Anomalous splitting of the $F_{1u}(\rightarrow 3F_u)$ vibrations in single-crystal C_{60} below the orientational-ordering transition," Phys. Rev. B **49**, 7052–7055 (1994).
[35]G. B. Alers, B. Golding, A. R. Kortan, R. C. Haddon, and F. A. Theil, "Existence of an orientational electric dipolar response in C_{60} single crystals," Science **257**, 511 (1992).
[36]L. Abouaf-Marguin, A.-M. Vasserot, C. Pardanaud, and X. Michaut, "Nuclear spin conversion of H_2O@C_{60} trapped in solid xenon at 4.2 K: A new assignment of ν_2 rovibrational lines," Chem. Phys. Lett. **480**, 82–85 (2009).
[37]S. Mamone, M. Concistrè, E. Carignani, B. Meier, A. Krachmalnicoff, O. G. Johannessen, X. Lei, Y. Li, M. Denning, M. Carravetta, K. Goh, A. J. Horsewill, R. J. Whitby, and M. H. Levitt, "Nuclear spin conversion of water inside fullerene cages detected by low-temperature nuclear magnetic resonance," J. Chem. Phys. **140**, 194306 (2014).
[38]C. C. Homes, P. J. Horoyski, M. L. W. Thewalt, B. P. Clayman, and T. R. Anthony, "Effect of isotopic disorder on the F_u modes in crystalline C_{60}," Phys. Rev. B **52**, 16892–16900 (1995).
[39]R. N. Zare, *Angular Momentum*, Baker Lecture Series (John Wiley & Sons, Inc., 1988).
[40]P. P. Bunker and P. Jensen, *Molecular Symmetry and Spectroscopy*, 2nd ed. (NRC of Canada, 1998), p. 747.
[41]D. A. Varshalovich, A. N. Moskalev, and V. K. Khersonskii, *Quantum Theory of Angular Momentum* (World Scientific, 1988).
[42]C. Cohen-Tannoudji, B. Diu, and F. Laloë, *Quantum Mechanics* (John Wiley & Sons, 2005).
[43]J. Verhoeven and A. Dymanus, "Magnetic properties and molecular quadrupole tensor of the water molecule by beam-maser Zeeman spectroscopy," J. Chem. Phys. **52**, 3222–3233 (1970).
[44]S. L. Altmann and P. Herzig, *Point-Group Theory Tables*, 2nd ed. (University of Vienna, Vienna, 2011).
[45]W. H. Shaffer, "Degenerate modes of vibration and perturbations in polyatomic molecules," Rev. Mod. Phys. **16**, 245–259 (1944).
[46]D. L. Dexter, "Absorption of light by atoms in solids," Phys. Rev. **101**, 48–55 (1956).
[47]Solid C_{60} has strong optical phonons between 500 and 1400 cm^{-1}. The index of refraction above 1400 cm^{-1} is 2.0 (Ref. 38). Using the phonon data from Table II (Ref. 38) and Eq. (1) (Ref. 38), we calculate the index of refraction at 50 cm^{-1}, $\eta = \sqrt{\Re[\varepsilon]} = 2.01$. Thus, $\eta = 2.0$ is a good approximation for the index of refraction in the frequency range of H_2O transitions reported here.
[48]S. Aoyagi, N. Hoshino, T. Akutagawa, Y. Sado, R. Kitaura, H. Shinohara, K. Sugimoto, R. Zhang, and Y. Murata, "A cubic dipole lattice of water molecules trapped inside carbon cages," Chem. Commun. **50**, 524–526 (2014).
[49]I. E. Gordon, L. S. Rothman, C. Hill, R. V. Kochanov, Y. Tan, P. F. Bernath, M. Birk, V. Boudon, A. Campargue, K. V. Chance, B. J. Drouin, J.-M. Flaud, R. R. Gamache, J. T. Hodges, D. Jacquemart, V. I. Perevalov, A. Perrin, K. P. Shine, M.-A. H. Smith, J. Tennyson, G. C. Toon, H. Tran, V. G. Tyuterev, A. Barbe, A. G. Császár, V. M. Devi, T. Furtenbacher, J. J. Harrison, J.-M. Hartmann, A. Jolly, T. J. Johnson, T. Karman, I. Kleiner, A. A. Kyuberis, J. Loos, O. M. Lyulin, S. T. Massie, S. N. Mikhailenko, N. Moazzen-Ahmadi, H. S. P. Müller, O. V. Naumenko, A. V. Nikitin, O. L. Polyansky, M. Rey, M. Rotger, S. W. Sharpe, K. Sung, E. Starikova, S. A. Tashkun, J. V. Auwera, G. Wagner, J. Wilzewski, P. Wcisło, S. Yu, and E. J. Zak, "The HITRAN 2016 molecular spectroscopic database," J. Quant. Spectrosc. Radiat. Transfer **203**, 3–69 (2017).
[50]J. Tennyson, N. F. Zobov, R. Williamson, O. L. Polyansky, and P. F. Bernath, "Experimental energy levels of the water molecule," J. Phys. Chem. Ref. Data **30**, 735 (2001).
[51]P. M. Felker and Z. Bačić, "Flexible water molecule in C_{60}: Intramolecular vibrational frequencies and translation-rotation eigenstates from fully coupled nine-dimensional quantum calculations with small basis sets," J. Chem. Phys. **152**, 014108 (2020).
[52]A. Varadwaj and P. R. Varadwaj, "Can a single molecule of water be completely isolated within the subnano-space inside the fullerene C_{60} cage? A quantum chemical prospective," Chem. - Eur. J. **18**, 15345–15360 (2012).
[53]A. B. Farimani, Y. Wu, and N. R. Aluru, "Rotational motion of a single water molecule in a buckyball," Phys. Chem. Chem. Phys. **15**, 17993–18000 (2013).
[54]H. Friedmann and S. Kimel, "Theory of shifts of vibration–rotation lines of diatomic molecules in noble-gas matrices. Intermolecular forces in crystals," J. Chem. Phys. **43**, 3925–3939 (1965).
[55]M. Xu, F. Sebastianelli, Z. Bačić, R. Lawler, and N. J. Turro, "H_2, HD, and D_2 inside C_{60}: Coupled translation-rotation eigenstates of the endohedral molecules from quantum five-dimensional calculations," J. Chem. Phys. **129**, 064313 (2008).
[56]R. A. Toth, "ν_2 band of $H_2{}^{16}O$: Line strengths and transition frequencies," J. Opt. Soc. Am. B **8**, 2236–2255 (1991).
[57]S. A. Clough, Y. Beers, G. P. Klein, and L. S. Rothman, "Dipole moment of water from Stark measurements of H_2O, HDO, and D_2O," J. Chem. Phys. **59**, 2254–2259 (1973).
[58]J. M. Flaud and C. Camy-Peyret, "Vibration-rotation intensities in H_2O-type molecules application to the $2\nu_2$, ν_1, and ν_3 bands of $H_2{}^{16}O$," J. Mol. Spectrosc. **55**, 278–310 (1975).
[59]C. Camy-Peyret and J.-M. Flaud, "Line positions and intensities in the ν_2 band of $H_2^{16}O$," Mol. Phys. **32**, 523–537 (1976).
[60]C. N. Ramachandran and N. Sathyamurthy, "Water clusters in a confined nonpolar environment," Chem. Phys. Lett. **410**, 348–351 (2005).
[61]K. Yagi and D. Watanabe, "Infrared spectra of water molecule encapsulated inside fullerene studied by instantaneous vibrational analysis," Int. J. Quantum Chem. **109**, 2080 (2009).
[62]P. A. Heiney, "Structure, dynamics and ordering transition of solid C_{60}," J. Phys. Chem. Solids **53**, 1333–1352 (1992).
[63]B. Sundqvist, "Fullerenes under high pressures," Adv. Phys. **48**, 1–134 (1999).
[64]D. L. Albritton, A. L. Schmeltekopf, and R. N. Zare, "An introduction to the least-square fitting of spectroscopic data," in *Molecular Spectroscopy: Modern Research* (Academic Press, Inc., New York, 1976), pp. 1–67.